BACHELOR' S THESIS / BIOMEDICAL ENGINEERING 2023

In-silico models of arteriovenous fistulas in patients with end-stage renal disease

Lídia Martínez Dalmau

upf. Universitat Pompeu Fabra Barcelona

Parc Taulí Institut d'Investigació i Innovació I3PT

In-silico models of arteriovenous fistulas in patients with end-stage renal disease

Lídia Martínez Dalmau

Bachelor's Thesis UPF 2022/2023

Thesis Supervisors:

Dr. Andy L. Olivares , Department of Information and Communication Technologies (DTIC)

Dr. José Ibeas , Parc Taulí Hospital Universitari

upf. Universitat Pompeu Fabra Barcelona
Parc Taulí Institut d'Investigació i Innovació I3PT

Acknowledgments

I would like to express my sincerest gratitude and appreciation to my thesis supervisors, Dr. Andy L. Olivares and Dr. José Antonio Ibeas, for their guidance and invaluable support during the entire duration of this thesis. I am truly grateful to Dr. Ibeas for granting me the opportunity to work in a clinical setting and witness the beauty of biomedical engineering within the hospital. My gratitude also extends to Dr. Óscar Cámara for his feedback and expertise. I would also like to acknowledge the contributions of Miriam Caravaca for always being willing to lend a helpful hand, especially in the data acquisition process. Furthermore, I would like to thank Carlos Albors for his assistance with loading the simulations.

Last but not least, I want to express my deepest admiration to my family and friends for the boundless encouragement I have received from them throughout my life.

Summary/Abstract

End-stage renal disease (ESRD) is a life-threatening condition that affects over 10% of the global population, necessitating hemodialysis (HD) for patients awaiting a kidney transplant. The arteriovenous fistula (AVF) is the preferred access for HD treatment, but it is often prone to complications that jeopardize its effectiveness and pose serious risks like thrombosis. AVF failure primarily stems from non-maturation of the AVF and post-maturation stenosis. Previous *in-silico* studies have suggested that these events are influenced by changes in the vascular lumen cross-sectional area and the degree of the anastomotic angle, which could be correlated with the patient's inflammatory state. However, literature on this subject is limited, focusing solely on individual patient-specific models in Computational Fluid Dynamics (CFD) simulations, neglecting specific boundary conditions and the patients' health status. This study aims to establish a foundation for constructing an advanced numerical model that accounts for the clinical, hemodynamic, and morphological characteristics of patients. It includes nine patient-specific geometries, with CFD simulation results presented for three of them while the others are still being analyzed. The models were created based on Magnetic Resonance Imaging (MRI) obtained at three time periods (1 week, 1 month, and 6 months) after surgery, which are critical for understanding the development and temporal evolution of the AVF. Boundary conditions were derived from ultrasound scans taken at these specific time points. Additionally, a mathematical 3-element Windkessel model was utilized, taking into account the patient's classification as normotensive or hypertensive to estimate its parameters. No previous study has examined such a large number of patients or conducted a comprehensive temporal follow-up while also considering the patients' health status. Specific AVF geometries and their evolution over time were found to impact the flow characteristics in patients. The juxta-anastomotic section was identified as the area most affected by flow in cases where the angle of the anastomosis was not tortuous describing a 'U-shape', exhibiting higher magnitude and distribution of Wall Shear Stress (WSS) and greater velocity magnitude.

Keywords

Arteriovenous fistula, Venous access, Hemodialysis (HD), Computational fluid dynamics (CFD), Numerical methods, Patient-specific model, 3-element Windkessel model

Index

1 Introduction **1**
- 1.1 Clinical background . . . 1
- 1.2 State of the art in numerical models for arteriovenous fistulas . . . 4
- 1.3 Aim of the project . . . 6

2 Methods **7**
- 2.1 Clinical characterization of the study . . . 7
- 2.2 MRI acquisition and segmentation . . . 8
- 2.3 Meshing . . . 9
  - 2.3.1 Surface mesh post-processing . . . 9
  - 2.3.2 Volume mesh generation . . . 10
- 2.4 Numerical simulations . . . 11
  - 2.4.1 Mesh convergence study . . . 11
  - 2.4.2 Time step convergence study . . . 12
  - 2.4.3 Solver specifications . . . 12
  - 2.4.4 Modeling assumptions and boundary conditions . . . 13
- 2.5 The 3-element Windkessel model as a boundary condition for the outflow vein . . . 14
  - 2.5.1 Model definition . . . 14
  - 2.5.2 Mathematical implementation . . . 15
  - 2.5.3 Parameter estimation . . . 16

3 Results **16**
- 3.1 Mesh convergence study . . . 16
- 3.2 Time step convergence study . . . 18
- 3.3 Results from the 3-element Windkessel model . . . 18
- 3.4 Temporal follow-up simulations: identified patterns . . . 20
- 3.5 Morphological parameters from arteriovenous fistulas segmentations . 22

4 Discussion **23**
- 4.1 Mesh convergence study . . . 23
- 4.2 Time step convergence study . . . 24
- 4.3 Indentified patterns from the temporal follow-up . . . 25
- 4.4 Morphological parameters correlated with arteriovenous fistula hemodynamics . . . 26
- 4.5 Limitations and future work . . . 27
  - 4.5.1 Raw data . . . 27
  - 4.5.2 Towards an enhanced computational model . . . 28
  - 4.5.3 Towards clinical applications . . . 29

5 Conclusion **30**

References **31**

A Appendix **37**
A.1 Mesh convergence study 38
A.2 Temporal follow-up simulations 41
A.3 Training course certificate 43

List of Figures

1 Blood circuit during hemodialysis treatment (image retrieved from [3]). 1

2 The venous access (i.e., the AVF) in the patient's forearm serves as a connection point to the dialysis machine, corresponding to the real anatomical structure on the right (the illustrations were retrieved from [10] and the anonymized image was provided by the dialysis department at Hospital Universitari Parc Taulí). 2

3 Significance of the different time periods in the AVF maturation process for its physiopathology [7]. 6

4 Pipeline followed to perform Computational Fluid Dynamics (CFD) simulations. 7

5 3D Slicer screenshot from the MRI corresponding to patient 6 in the 6-month time period. **(a)** It shows the vascular anatomy of the middle arm: the radiocephalic bifurcation. The vein is easily identified because of its superficial location, and the artery is localized within the muscle and can be recognized by its 'Mickey Mouse'-shape. The round shapes on the sides of the artery are the satellite veins. **(b)** The radiocephalic AVF is the only one located in the distal part of the arm, which can be identified by the presence of the radius and ulna. 9

6 Temporal evolution in the geometry of the AVF for Patient 8. 10

7 Schematic of the BCs used in the numerical model. Two velocity profiles are applied as inlets in the proximal artery (PA) and distal artery (DA). The 3-element Windkessel model is applied for a pressure outlet in the outflow vein (OV). 13

8 3-element Windkessel model circuit. 15

9 Average velocity and WSS results of the mesh convergence study for different mesh densities (i.e., Δx) in the outflow vein and yuxtaanastomotic zones. The exact area that was analyzed can be seen in the Appendix A. 17

10 Morphological distribution of WSS for different mesh densities representative of the mesh convergence study. 18

11 Data from Patient 6, 6 months. **(a)** Velocity waveforms for the proximal (PA) and distal (DA) segments of the artery, which are inlet BCs, and also inputs for the WK, as they are used to compute the flow. **(b)** Outlet pressure wavefrom in the outflow vein resulting from the WK model. 19

12 Velocity pathlines in the different geometries for one week. The pathline pattern is repeated for one month and six months. 20

13 Temporal evolution of WSS distribution in the different AVFs. . . . 21

14 Element distribution for several mesh densities. 23

15 All the surface meshes of the patients involved in the study except for patient 8, which is already shown in Figure 6. 37

16 Sections of the juxta-nastomotic zone and outflow vein analyzed for drawing conclusions in this study. 38

17 Average pressure results of the mesh convergence study for different mesh densities (i.e., Δx) in the yuxta-anastomotic zone. 38
18 Average pressure results of the mesh convergence study for different mesh densities (i.e., Δx) in the outflow vein zone. 39
19 Average velocity results of the mesh convergence study for different mesh densities (i.e., Δx) in the outflow vein BC. 39
20 Average pressure and WSS results of the mesh convergence study for different mesh densities (i.e., Δx) at the proximal artery BC. 40
21 Average pressure and WSS results of the mesh convergence study for different mesh densities (i.e., Δx) at the distal artery BC. 40
22 Geometry of the AVF corresponding to patient 6, 1 week. In this, the pathlines depict the contribution of different segments of the artery (PA and DA) to the vein flow (OV). These illustrations demonstrate the flow split assumption applied in the contours, where PA contributes 75% of the flow to OV, and DA contributes 25%. The dynamics of the pathlines is almost the same for all cases and all simulated times due to the BCs applied. 41
23 Magnitude of velocity vectors in AVF flow in Patient 1, week 1 (a, b, c) and month 1 (d, e, f). The results for the 6-month simulation are very similar to those of the 1-month simulation, so they have not been included to avoid redundancy. This extends to the other patient cases. 42
24 Theoretical-practical course 'Ultrasound for Vascular Access in Hemodialysis' certificate of attendance. 43

List of Tables

1 Synthesis of the state of the art of the literature so far on CFD simulations for AVF. Acronyms: 'PS' stands for 'Patient-Specific', 'ND' stands for 'Not Described', '-p-' stands for 'pressure', 'v-' stands for 'velocity', and 'GCI' stands for 'Grid Convergence Index'. 4

2 Types of artery-vein connection of the AVFs of the patients in the study. 8

3 Clinical data from all patients involved in the study, including AVF characterization and hemodynamic parameters. Acronyms: 'SP' stands for 'Systolic Pressure', 'DP' stands for 'Diastolic Pressure', 'MP' stands for 'Mean Pressure', and 'HT' stands for 'Hypertension'. . . . 8

4 Volume mesh characteristics. 11

5 Change in residual values according to each volume mesh density. . . 16

6 Time step convergence study results according to the CFL condition. 18

7 3-element Windkessel estimated model parameters. 'NA' stands for 'Not Available', meaning that the ultrasound for BC extraction for that time period in that particular patient was not available. 19

8 Physical parameters of the AVF for different patients (1, 6 and 8). 'YAS' stands for 'yuxtaanastomotic' and 'OV' for 'outflow vein'. . . . 20

9 Mean Reynolds number (Re) in the outflow vein and juxta-anastomotic zones. 21

10 Morphological data from all the AVFs segmented in the study. The diameter of the anastomosis refers to the diameter at the binding site. 22

1 Introduction

1.1 Clinical background

End-stage renal disease (ESRD), also known as end-stage kidney disease (ESKD), is the final stage of chronic kidney disease (CKD). ESRD presents a significant global health challenge that is rapidly increasing and placing a substantial burden on healthcare systems. Impacting over 10% of the global population, ESRD affects more than 800 million individuals [1]. It is characterized by advanced renal deterioration, which causes the kidneys to become unable to filter water, leading to the accumulation of electrolytes, toxic wastes, and water in the bloodstream. These events endanger other organs in the body and make ESRD a life-threatening condition [2].

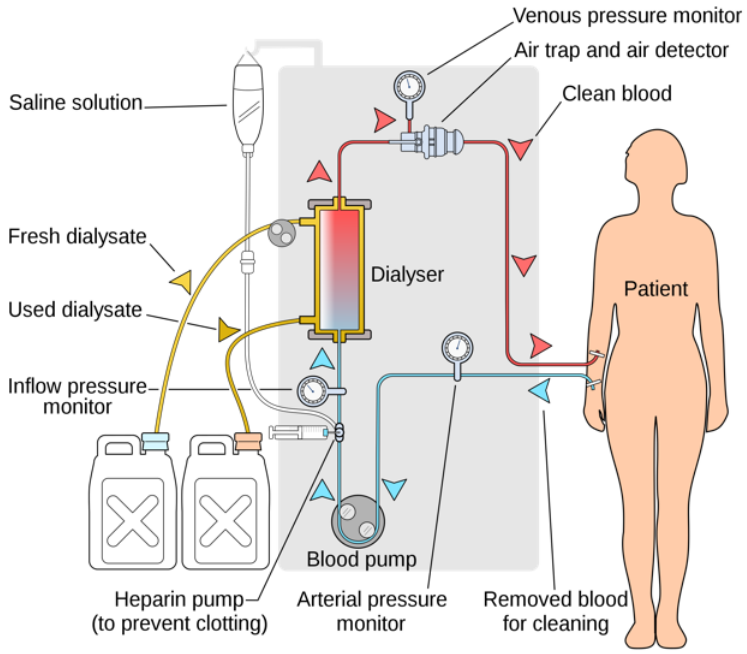

Figure 1: Blood circuit during hemodialysis treatment (image retrieved from [3]).

The only treatment options for renal failure are kidney transplant or dialysis. In Spain, the approximate average waiting time for a kidney transplant is 2.5 years [4], while in the US, it is 3.6 years [4]. Therefore, most patients need to undergo dialysis while waiting for a transplant. Hemodialysis (HD) is the most commonly used type of dialysis [5], in which a venous access called arteriovenous fistula (AVF) is required to connect the patient to the dialysis machine (see Figure 1). This is done by means of two needles: one for the inflow of blood to be filtered and the other for the outflow of cleaned blood to be returned to the body (see Figure 2) [6][7].

There are two types of AVF: native arteriovenous fistulas (nAVFs) and grafts. nAVFs are created by surgically connecting an artery and a vein without synthetic implants, a union medically termed 'anastomosis' [7]. nAVFs are the most durable

and have the lowest risk of infection compared to non-native access techniques [7][8][9].

AVFs are usually created on the patient's non-dominant forearm due to its easy accessibility for HD treatment, which is received at least three times a week [7]. Its configuration depends on which vein and artery are selected for splicing [8]. The most common nAVFs are the radio-cephalic fistula (radial artery - cephalic vein anastomosis), the brachial-cephalic fistula (upper arm cephalic vein - brachial artery anastomosis), and the brachial-basilic fistula (basilic vein - brachial artery anastomosis) [7][8][9].

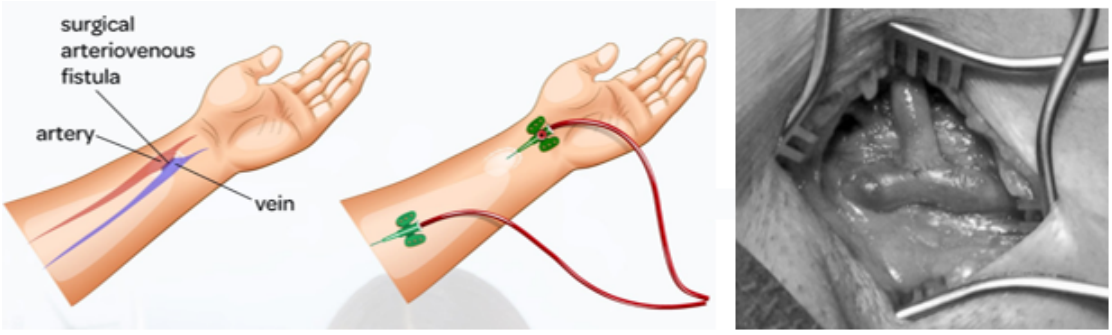

Figure 2: The venous access (i.e., the AVF) in the patient's forearm serves as a connection point to the dialysis machine, corresponding to the real anatomical structure on the right (the illustrations were retrieved from [10] and the anonymized image was provided by the dialysis department at Hospital Universitari Parc Taulí).

The main indicators for AVF surgery are an estimated glomerular filtration rate (eGFR) lower than 15 mL/min/1.73 m^2 or an estimation to perform the first HD session within the next 6 months, as nAVFs require 2 to 4 weeks to mature [7]. Maturation refers to the AVF being capable of delivering sufficient blood flow for an adequate HD treatment, which cannot be achieved under physiological conditions. The anastomosis allows blood to flow directly from the artery (a vascular entity characterized by high pressure and low capacitance) into the vein (a vascular entity characterized by low pressure and high capacitance) [11], increasing the blood pressure and causing the vein walls to enlarge, enabling it to supply the necessary increased blood flow up to approximately 1000 mL/min [7].

This phenomenon is known as arterialization of the vein and lasts approximately 6 to 8 weeks [11]. The AVF can increase the flow in the arterialized vein by up to 100 times compared to the normal flow of vessels before vascular surgery. The pre-surgical average flow of the cephalic and basilic veins, which are typically used for nAVF creation, is 5 mL/min, while the feeding brachial and radial arteries have pre-surgical flows of 75 - 100 mL/min and 50 mL/min, respectively [7]. An AVF is considered optimal for HD when its flow is at least 500 mL/min in the maturation stage, and the fistula lumen has a diameter of at least 4 mm [7].

Arterialization requires the vein to be exposed to an elevated pressure gradi-

ent, increased blood flow, and high oscillating wall shear stress (WSS) caused by blood friction against the vessels and subsequent circumferential vessel deformation [12][13]. Endothelial cells (ECs) in the AVF have WSS-sensitive mechanoreceptors. Studies carried out in the last decade [12][14] have correlated high values of WSS with an enhanced release of nitric oxide (NO) in quiescent ECs, whereas low values are attributed to reduced levels of NO in ECs. AVF linear unbent areas typically present laminar flow (e.g., the arterial tree) and are associated with high WSS. Conversely, areas of bifurcation or curvature on the nAVF, typically presenting turbulent flow (e.g., the anastomosis), are associated with low WSS [15][16].

The upregulation of NO leads to a downregulation of both proinflammatory and proliferative genes, which produce minor atherosclerotic lesions. However, the downregulation of NO results in the upregulation of proliferative, proinflammatory, and prothrombotic genes, responsible for neointimal hyperplasia (NH) [12][13]. NH leads to stenosis due to deficient outward venous remodeling, including both vasodilation and structural modifications of the nAVF vein [11][17]. These stressors on the ECs often result in the nAVF being unable to provide the desired HD flow (i.e., $\geq$ 500 mL/min) [7]. This scenario can occur during the maturation of the nAVF or post-maturation, and it is an indicator of pathology known as AVF failure.

Although the main inducers of AVF failure appear to be structural and functional changes in the vascular wall, the pathophysiology of AVF failure is still not fully understood. Several theories have been proposed, mostly related to the onset of NH. The most widely accepted theory is that hemodynamic pressure in the AVF activates the immune system, triggering the abovementioned inflammatory state that leads to the development of NH [18]. What remains unknown are the precise driver(s) of this mechanism, as well as the conditions under which it is initiated. One hypothesis suggests that AVF failure is influenced by the initial surgical trauma, while another posits that pre- and post-surgery inflammation levels play a significant role in AVF maturation and success. Furthermore, the configuration of the AVF is considered, including morphological parameters such as AVF length and caliber, the position of the artery-vein anastomosis, and the presence of bifurcations, as potential risk factors. Additionally, it is theorized that repeated puncture during hemodialysis (HD), combined with chronic exposure to physiologically turbulent and high-magnitude flow with shear forces, may contribute to AVF dysfunction by adversely affecting its condition [18][19][20][21][11].

The most common complications of AVFs include thrombosis resulting from stenosis, congestive heart failure, ischemic neuropathy, steal syndrome, and aneurysms [22]. These can require surgical revision, surgery for a secondary nAVF, or even an endovascular procedure for angioplasty rescue, among others [7]. The last published meta-analysis on AVF efficacy and safety outcomes (Bylsma et al., 2017) [23] estimated a primary unassisted patency rate (i.e., a measure of how effectively a blood vessel remains unobstructed following a first surgical procedure) of 64% for the nAVF and a secondary patency rate (i.e., a measure of how effectively a previously treated blood vessel remains unobstructed after a re-intervention) of 79%, both one year

post-operation. As a rule, patency is the state of unobstructed flow within a blood vessel. Moreover, hospitalizations due to AVF failure account for 25% of admissions worldwide [24].

Since stressors related to AVF failure appear to have a greater impact depending on the distribution of mechanical impacts of blood on the AVF anatomical structure [12], tools aimed at a hemodynamic-morphological study could reveal AVF configurations that are more prone to failure. To achieve this objective, research has focused on image processing and computational models over the last two decades [25].

1.2 State of the art in numerical models for arteriovenous fistulas

The main computational strategies for analyzing AVF hemodynamics are based on Computational Fluid Dynamics (CFD). Table 1 presents a summary of the most notable studies along with their corresponding descriptions of the numerical models.

Ref.	Mesh characteristics		Model specifications			Grid verification
	Geometry	Elements	Walls	Vein BC	Flow	
[26]	PS	4.3M	Rigid	0-pressure	non-Newtonian	GCI test
[27]	PS	ND	Dynamic	gauge-p	ND	Yes (no details)
[11]	PS	4M	Dynamic	WK	Newtonian	GCI test
[14]	PS	344k	Mixed	ND	non-Newtonian	Yes (no details)
[28]	PS	1.7M	Rigid	traction-free	turbulent	WSS-based
[2]	PS	3.5M	Rigid	ND	ND	Yes (no details)
[13]	PS	ND	Dynamic	WK	Newtonian	ND
[29]	PS	13.68M	Rigid	p-waveform	non-Newtonian	Yes (no details)
[30]	Ideal	300k	Dynamic	ND	non-Newtonian	Yes (no details)
[31]	Ideal	1.7M	Rigid	traction-free	Newtonian	Relative to finest grid
[18]	PS	300k	Rigid	traction-free	non-Newtonian	Relative to finest grid
[32]	Ideal	1.7M	Rigid	traction-free	Newtonian	Yes (no details)
[33]	PS	3.2M	Rigid	ND	non-Newtonian	Yes (no details)
[34]	PS	873k	Dynamic	p-waveform	non-Newtonian	Yes (no details)
[21]	PS	6.23M	Dynamic	ND	Newtonian	Yes (no details)
[19]	PS	0.25M	Rigid	flow rate	Newtonian	Yes (no details)
[20]	PS	0.9M	Rigid	v-waveform	Newtonian	WSS-based
[35]	Ideal	ND	Rigid	flow rate	non-Newtonian	ND
[36]	Ideal	ND	Rigid	ND	non-Newtonian	ND
[37]	PS	350k	Rigid	ND	Newtonian	Yes (no details)
[38]	Ideal	ND	Rigid	traction-free	Newtonian	Relative to finest grid
[25]	PS	ND	Rigid	ND	non-Newtonian	Peak flow rate-based

Table 1: Synthesis of the state of the art of the literature so far on CFD simulations for AVF. Acronyms: 'PS' stands for 'Patient-Specific', 'ND' stands for 'Not Described', '-p-' stands for 'pressure', 'v-' stands for 'velocity', and 'GCI' stands for 'Grid Convergence Index'.

CFD studies related to AVFs published to date can be classified into two categories: ideal models and patient-specific models. Ideal models are generated in

Computer-Aided Design (CAD) software and primarily focus on analyzing the impact of specific morphological parameters, such as the angle of the anastomosis and the cross-sectional area, on the flow behavior [30][14][12][39][35]. However, one challenge with ideal models is that the values of these parameters are often obtained from sources that are not validated by medical professionals, leading to potentially incorrect or clinically irrelevant results. For instance, analyzing obtuse angles between the artery and the anastomosed vein may not represent significant problems or may be uncommonly observed in patients undergoing HD.

In fact, Lee et al. (2016) [30] published an article which had the main result of correlating a more obtuse anastomotic angle with lower WSS values. The authors employed a Fluid-Structure Interaction (FSI) model of changing elastic walls according to blood pressure in a cardiac cycle. They defined blood as a non-Newtonian fluid and used the low Reynolds number k-ε turbulence model to better characterize the transition from laminar to turbulent flow. This version enhances the accuracy of the classical k-ε turbulence model in the region close to the wall, where viscous effects dominate [40].

Other ideal studies, such as Browne et al. (2015), describe the walls as rigid, which is the most common approach in ideal models. In rigid-wall patient-specific CFD simulations, Decorato et al. (2011) [41] discovered that WSS was overestimated by 10-13%. In a separate study by Alam et al. (2022) [27], it was observed that both rigid and elastic models displayed comparable non-dimensional velocity patterns, with the highest velocity occurring at the anastomosis in both cases. However, in terms of magnitude, rigid geometries underestimated the non-dimensional velocity by approximately 8%. In addition, in the article by Browne et al. (2015) [17], blood was established as an incompressible Newtonian fluid. Generally, in terms of fluid description, there is much discrepancy regarding its definition as Newtonian or non-Newtonian (see Table 1).

To comprehensively study the failure of AVFs, a multifactorial investigation encompassing hemodynamic and morphological parameters is required [16][42]. Patient-specific models are regarded as the standard approach for this purpose. Many of these models incorporate retrograde flow and use time-dependent boundary conditions (BCs) that represent velocity profiles corresponding to 2 to 4 cardiac cycles. Estimation of the exit pressure at the venous access commonly employs a lumped model. Alternatively, it is frequently assumed to be 0. Another feasible choice for the BC at the outflow vein is the traction-free condition. Both the 0-pressure and traction-free conditions are convenient options when data for a BC cannot be acquired (see Table 1).

Many authors (such as [26]; [14]; [43]; [44]) also define the flow type according to the Shear Stress Transport (SST) k-ω turbulence model. It adapts to specific (i.e., local) flow conditions, by enabling a seamless transition between turbulent behaviors near the wall, where boundary layer phenomena and viscous effects dominate, and in regions away from the wall, where the flow is typically more homogeneous and

less influenced by the presence of solid boundaries [45].

Literature so far has attempted to generate a complex computational model of flow in the AVF. For this purpose, different modeling assumptions, different BCs, and different parameters have been analyzed (as illustrated in Table 1). The vast majority of articles focus on the anatomical distribution of WSS, on the pressure drop in the AVF structure, or simply on validating *in-silico* flow values against physiological ones. However, these results have rarely been applied in hospitals.

The challenge of applying CFD studies to clinical practice is rooted in the difficulty of obtaining experimental data for validation of the simulation results, such as the internal pressure of AVF vessels. Additionally, constructing a numerical model is a demanding task, due to the inherent nonlinearity and complex behavior of AVF's non-physiological flow. Furthermore, the fact that most studies are conducted solely from an engineering standpoint results in models that are not significant in a medical environment. Moreover, there is a lack of patient-specific data, as no studies have examined more than one patient or evaluated the temporal maturation of AVF.

1.3 Aim of the project

1 week post-surgery	**Healing of the surgical site:** inflammation resolution, early stages of vascular remodeling, and first exposure to non-physiological hemodynamics.
1 month post-surgery	**Milestone for AVF maturation assessment:** changes in the vessel structure play a crucial role in the long-term success of the AVF.
6 months post-surgery	**Advanced stage of AVF maturation:** the intima should have reached a stable and functional state, serving as an indicator of long-term viability of the AVF.

Figure 3: Significance of the different time periods in the AVF maturation process for its physiopathology [7].

The main objective of this project has been the creation of a computational model of the AVF using Magnetic Resonance Imaging slices (MRIs) of patients with ESRD at different post-surgery periods: 1 week, 1 month, and 6 months. These periods are critical for the development of its anatomical structure, which could serve to identify patterns correlated with its functional failure (see Figure 3). Thereby, efforts were focused on the following tasks:

1. Extracting specific boundary conditions from ultrasounds when available and using them to generate unavailable ones through mathematical models.

2. Verifying mesh density and time step through convergence analysis.

3. Generating patient-specific models for all patients in all time-tracked periods to set up and run CFD simulations.

4. Correlating AVF failure with AVF hemodynamics and morphological affection of the AVF structure.

2 Methods

This section describes the overall workflow carried out during the project. Details of the intermediate steps will be given in the different subsections as well as in the Appendix A.

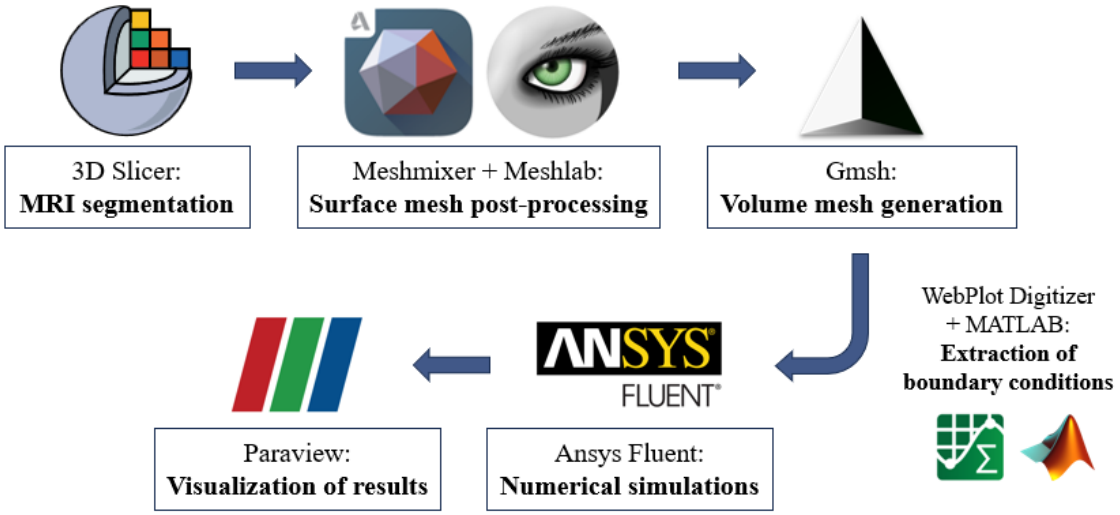

Figure 4: Pipeline followed to perform Computational Fluid Dynamics (CFD) simulations.

2.1 Clinical characterization of the study

This work has been conducted within the 'Clinical, Interventional, and Computational Nephrology' (CICN) group of the 'Institut d'Investigació i Innovació Parc Taulí' (I3PT) in Sabadell, Barcelona, Spain. The data collection for this study began in 2019 but was interrupted by the COVID-19 pandemic. In total, nine patients remained in the study and underwent three MRI scans at the specified time points mentioned in the preceding section 1.3. Prior to commencing the workflow, the data were anonymized using the *Python's dicognito* module [1], performed by CICN's engineer Miriam Caravaca. Each patient was assigned a number from 1 to 9, as can be seen in the 'ID' of Table 2, which specifies the type of AVF binding of each patient.

[1] https://www.python.org/

Table 3 specifies parameters that serve to characterize the pathophysiological state of the AVF. Specifically, the percentage of stenosis is determined by substracting the diameter at the narrowest point of the stenosis from the diameter at a reference point, which is generally located proximal to the stenosis.

Patient ID	AVF type
1	Radial–perforating
2	Brachial–perforating
3	Radiocephalic
4	Radiocephalic
5	Radiocephalic
6	Brachiocephalic
7	Radial–perforating
8	Radiocephalic
9	Brachial–perforating

Table 2: Types of artery-vein connection of the AVFs of the patients in the study.

ID	1 week		1 month		6 months		Pressure (mmHg)			
	Flux (mL/min)	Stenosis	Flux (mL/min)	Stenosis	Flux (mL/min)	Stenosis	SP	DP	MP	HT
1	1,000	No	1,200	No	-	No	139	94	109	No
2	700	No	1,200	No	1,500	No	140	48	78.67	No
3	400	No	350	No	500	No	135	85	102	No
4	850	60/70%	750	60/70%	750	60%	138	72	94	No
5	750	No	1,000	No	1,000	No	132	70	90.6	No
6	1,800	No	2,200	No	2,800	No	116	73	87.9	No
7	1,000	No	1,000	No	1,500	No	174	78	110	Yes
8	850	No	900	No	-	No	167	59	95	Yes
9	350	No	600	No	-	No	160	71	100.7	Yes

Table 3: Clinical data from all patients involved in the study, including AVF characterization and hemodynamic parameters. Acronyms: 'SP' stands for 'Systolic Pressure', 'DP' stands for 'Diastolic Pressure', 'MP' stands for 'Mean Pressure', and 'HT' stands for 'Hypertension'.

2.2 MRI acquisition and segmentation

Patient-specific AVF geometries were obtained from anonymized MRI acquired at Consorci Corporació Sanitària Parc Taulí (Sabadell, Spain) with a T3 scanner. All patients were in supine position during the acquisition process, which was produced within three different time intervals: 1 week, 1 month, and 6 months post AVF surgery. During time periods near the imaging procedure, typically within the same week, ultrasound scans were conducted on the AVF arm of the patients. The purpose of these was to gather hemodynamic data and identify the presence of stenosis, particularly juxta-anastomotic stenosis (i.e., located in the vicinity of the anastomosis). Subsequently, this information was utilized in constructing the model. All patients ivolved in the study had previously signed an informed consent, and the

research was approved by the hospital's ethics committee.

The resulting images were in DICOM (Digital Imaging and Communications in Medicine) format and had a voxel resolution of 0.3125 mm x 0.3125 mm x 1.0000 mm. The segmentation process was performed semi-automatically on *3D Slicer (version 5.0.2)* [2] by applying the built-in region-growing-based segmentation algorithm 'Grow from seeds' [46]. All segmentations were done by the author of this thesis, which were subsequently validated by Dr. Ibeas, the nephrologist co-supervisor of this thesis.

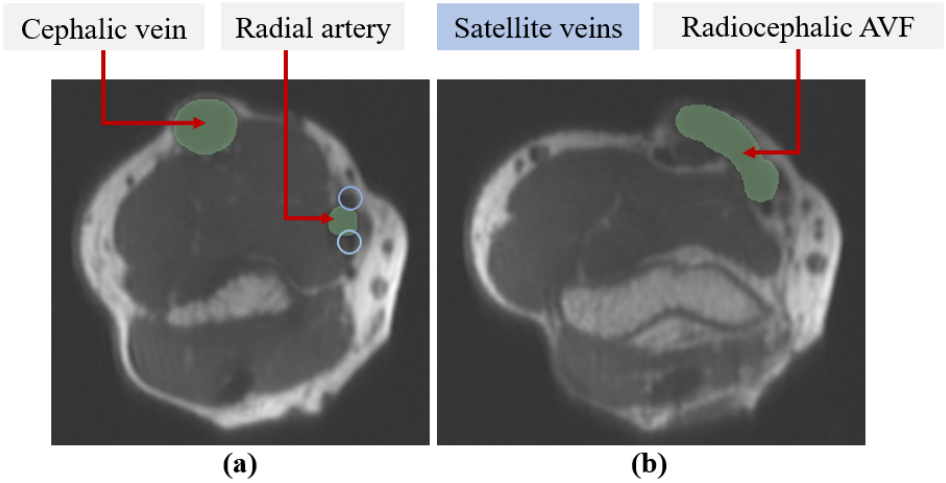

Figure 5: 3D Slicer screenshot from the MRI corresponding to patient 6 in the 6-month time period. **(a)** It shows the vascular anatomy of the middle arm: the radiocephalic bifurcation. The vein is easily identified because of its superficial location, and the artery is localized within the muscle and can be recognized by its 'Mickey Mouse'-shape. The round shapes on the sides of the artery are the satellite veins. **(b)** The radiocephalic AVF is the only one located in the distal part of the arm, which can be identified by the presence of the radius and ulna.

The selected anatomy includes the proximal (at least 50 mm from the anastomosis site) and distal (at least 15 mm from the anastomosis site) branches of the artery and the feeding vein attached to the artery via the anastomosis. The satellite veins accompanying the artery were excluded since they are not significant for the AVF hemodynamics.

2.3 Meshing

2.3.1 Surface mesh post-processing

After obtaining the segmentation from *3D Slicer*, it was imported into *Meshmixer (version 3.5.474)* [3] for post-processing. In *Meshmixer*, the resulting triangular unstructured surface mesh underwent refinement. This refinement process involved

[2] https://www.slicer.org/
[3] https://meshmixer.com/

smoothing rough areas from the segmentation and ensuring a uniform element distribution at the boundaries. This was achieved by reinforcing 'Face Normals' at the edge region to ensure a consistent and smooth transition between adjacent faces. Consequently, local filtering techniques were applied. *Meshmixer* was used in conjunction with *Meshlab (version 2020.02)* [4] to further refine the surface meshes and correct self-intersecting faces and non-manifold edges. The 'Taubin smooth' filter was employed to redistribute displaced vertices, aligning them more closely with the average position of their neighboring vertices [47]. Morphological parameters were also extracted using both *Meshmixer* and *Meshlab*.

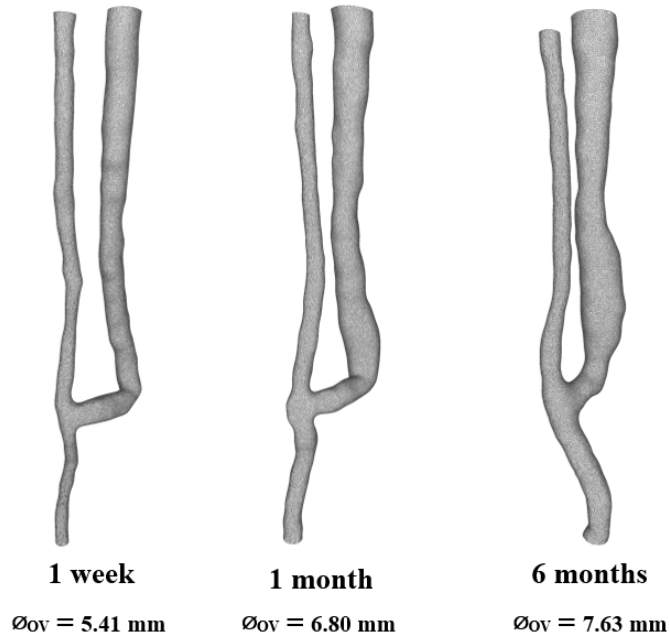

Figure 6: Temporal evolution in the geometry of the AVF for Patient 8.

2.3.2 Volume mesh generation

All surface meshes were subsequently converted to volume in *Gmsh (version 4.10.5)* [5] (see Figure 6). Considering the grid is unstructured, elements for the volume mesh were chosen as tetrahedrons rather than hexahedrons due to the greater adaptability of the tetrahedra to anatomical shapes. The built-in 'Netgen' meshing algorithm was operated to achieve good shape quality, size uniformity, and low distortion of the elements [48]. *Ansys Fluent (version 2019)* [6] was later on utilized to enhance mesh quality through the Text User Interface (TUI). The process involved iterative usage of TUI commands such as */mesh/refine* or */mesh/smooth* to locally improve the mesh until leaving only 0.5% or fewer elements in the volume mesh with a Minimum Orthogonal Quality (MOQ) of less than 0.01 [49].

[4] https://www.meshlab.net/
[5] https://gmsh.info/
[6] https://www.ansys.com/products/fluids/ansys-fluent

2.4 Numerical simulations

The presented study involves numerical simulations in the field of computational fluid dynamics (CFD) using the solver *Ansys Fluent (version 2019 R3)*. This software employs the finite volume method (FVM) technique to solve the Navier-Stokes governing equations [50] for mass conservation (Equation 1), and momentum conservation (Equation 2).

$$\vec{\nabla} \cdot \vec{U} = 0 \tag{1}$$

$$\rho \cdot \frac{\partial \vec{U}}{\partial t} + \rho(\vec{\nabla} \cdot \vec{U})\vec{U} = -\vec{\nabla}p + \mu\vec{\nabla}^2\vec{U} + \rho\vec{f_b} \tag{2}$$

In equations 1 and 2, U is the fluid velocity, p is the fluid pressure ρ is the fluid density, and μ is the fluid dynamic viscosity. The symbol $\vec{f_b}$ stands for body forces per unit mass.

2.4.1 Mesh convergence study

Multiple mesh densities from Patient 6, 6 months were analysed for the mesh convergence study (see Table 4). Taking literature as a reference, a 120k-element volume mesh consisting of tetrahedra was created on *Gmsh*. From this, two other principal meshes of approximately 740k and 6M elements each were created by splitting the original mesh elements by a factor of 2, which led to an increase in each consecutive mesh size by $\sim 2^3$. This criterion is based on the protocol followed by Khalili, Ehsan, et al. (2023) [51] in their study about good practices for CFD simulations on left atrial flows. In addition, volume meshes of densities from 463k to 171k were also used to represent intermediate values. These were made by creating a 75k element surface mesh from the original MRI segmentation. From this surface mesh, the number of elements was reduced by 5% consecutively, until a 35k surface mesh was achieved.

Mesh size (# elements)	$\sim \Delta$x (mm)
120k	0.93
171k	0.82
206k	0.77
249k	0.73
290k	0.69
338k	0.66
390k	0.63
422k	0.61
463k	0.59
740k	0.51
6M	0.25

Table 4: Volume mesh characteristics.

To demonstrate the independence of the results from the mesh density [52][53], WSS distribution, and mean velocities were evaluated. In order not to have highly distorted velocity and WSS values, the values of 0 were eliminated for the calculation of their averages. This is because the WSS is only represented on the AVF wall, and the velocity is 0 in this zone due to the no-slip condition. These parameters were numerically analyzed at the boundaries (which served as controls), at the juxta-anastomotic section, and at the proximal part of the OV. The juxta-anastomotic portion has been most closely related to fistula failure, and the OV is key because it is where flow is usually stabilized. In the PA and DA, velocity is a Dirichlet boundary condition, so in these only pressure and WSS were analyzed. In the OV, velocity was analyzed. In addition, residual values needed for the convergence of each mesh were taken into account, as well as the impact of mesh quality on the results.

2.4.2 Time step convergence study

The time step convergence study was performed according to the Courant-Friedrichs-Lewy (CFL) condition, as given by equation 3, where U represents the flow wave velocity, Δt is the time step, and Δx is the element edge [54][55]. For a time-marching solver, the time step, determined by the dimentionless term known as the Courant number (C) should be below 1 (i.e., $C_{max} \leq 1$). Since the BCs are a time-dependant and velocity values change along the geometry as flow develops, the highest mean velocity value was taken for the C_{max} calculations to ensure compliance with the CFL condition throughout the domain. The following time steps were tested: 1×10^{-4} sec, 5×10^{-4} sec, 1×10^{-3} sec, 5×10^{-3} sec, 1×10^{-2} sec, and 5×10^{-2} sec. The BCs used for this study were extracted from ultrasound images using *WebPlotDigitizer (version v4.6)* [7] and the extracted time function was extrapolated to each time step with *MATLAB (version R2022a)* [8].

$$C = U \cdot \frac{\Delta t}{\Delta x} \leq C_{max} \tag{3}$$

2.4.3 Solver specifications

The velocity formulation was classified as absolute, and the selected solver technology was pressure-based. For the latter, the algorithm scheme was set to be coupled to improve convergence, and the Rhie-Chow correction was employed to enhance accuracy when computing the continuity and momentum equations based on a momentum-based flux type. Gradients of the flow variables within the spatial discretization were approximated using the Green-Gauss node-based method.

For the mesh convergence study, simulations were run in steady mode. However, for the time step convergence study and final transient simulations, the transient mode was established. In these, the transient formulation chosen was second order implicit for enhanced stability. A total of 4 seconds were simulated, but analysis

[7] https://automeris.io/WebPlotDigitizer/
[8] https://es.mathworks.com/products/matlab.html

was only performed from the first second onwards to remove transients from the solution startup. The residual values for convergence were established to be below 0.001 for both steady and transient simulations. However, in the case of the steady simulations, the value of the residual for the continuity had to be increased to 0.05 to ensure convergence of the solution.

2.4.4 Modeling assumptions and boundary conditions

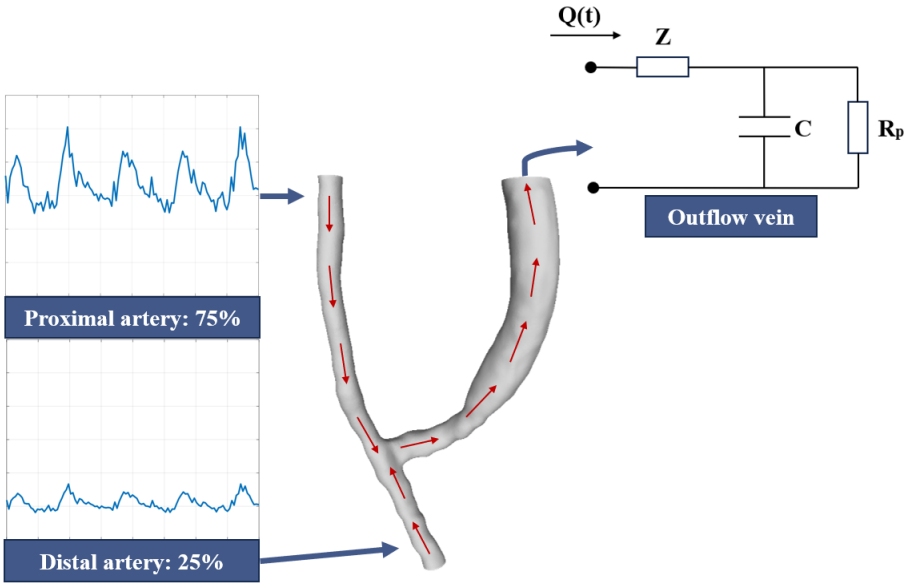

Figure 7: Schematic of the BCs used in the numerical model. Two velocity profiles are applied as inlets in the proximal artery (PA) and distal artery (DA). The 3-element Windkessel model is applied for a pressure outlet in the outflow vein (OV).

Modeling assumptions. In the AVF, blood mostly follows ordered parallel pathlines until it reaches the anastomosis area, where the Venturi effect is supposed to occur, causing the flow to become turbulent. Furthermore, since the compressibility of red blood cells is not significant, blood was approximated as an incompressible and Newtonian viscous laminar fluid with a density of $\rho = 1{,}050$ kg/m^3 and viscosity of $\mu = 0.0035$ kg/m·s [56]. The vascular tissue density was defined as $\rho = 1{,}102$ kg/m^3 [56]. The vascular walls were assumed to be rigid. Due to the small length scale of the roughness on both the artery and vein walls, their effect on the fluid dynamics was assumed to be negligible. The no-slip condition (i.e., zero velocity) was also applied at the vascular walls.

Boundary conditions. The normal flow pattern in the AVF moves from the artery towards the vein (see Figure 7). As a general rule, the proximal part of the artery contributes approximately 75% of the flow that enters the vein, while the distal part contributes 25%. This phenomenon, when implemented in the BCs, is known as the flow split assumption [26]. For the steady simulations, the inlet velocity in the PA was set as 0.75 m/s, and in the DA as 0.25 m/s. The outlet of the

OV was implemented as a pressure of 0. In contrast, for the time step convergence study and final transient simulations, the cardiac waveform for the PA was acquired from an AVF Doppler ultrasound taken at a time period close to the MRI imaging during the different analyzed time periods in this study. Since the velocity profile in the DA was not available, the flow split assumption was applied, where the distal waveform was obtained from the proximal one. These waveforms were introduced as inlets in the PA and DA. The BC for the OV was set to have 0 pressure in the time step convergence study, and a pressure profile obtained through a 3-element Windkessel model in the final transient simulations.

2.5 The 3-element Windkessel model as a boundary condition for the outflow vein

2.5.1 Model definition

The 3-element Windkessel (WK) model is a lumped-type model developed by a German physiologist named Otto Frank in the 1890s [57]. It describes the behavior of the arterial system by analogizing electronic circuit variables. Since the outflow vein (OV) of the AVF arterializes and takes on characteristics very similar to those of real arteries, this model can be applied as an outlet of the OV. Based on the understanding that the distensibility of the arterialized vessel enables it to dilate and store a portion of the blood from the AVF, resulting in a gradual increase in pressure, the model utilizes the flow within a specific geometry and establishes a correlation with its corresponding pressure. This correlation serves as an output of the model.

The three parameters that constitute the WK model are modeled as an impedance in series with a parallel combination of a capacitor and another resistor (see Figure 8). The capacitance (C) represents the compliance of the arterialized vein, while the parallel resistance signifies the peripheral resistance (R_p) to the passage of blood flow through the OV into the subsequent vascular system of the arm. The series impedance (Z) represents the propagation of the flow wave through the structure.

$$C = \frac{\Delta V}{\Delta P} \tag{4}$$

In equation 4, ΔV is the volume change produced in the OV when subjected to a certain pressure ΔP.

$$R_p = \frac{\Delta P}{\Delta Q} \tag{5}$$

Equation 5 is the isolation of R_p from the analogy of the Ohm's law, $\Delta\text{P} = \Delta\text{Q}\cdot R_p$.

$$Z = v \cdot \frac{\rho}{A_c} \tag{6}$$

In equation 6, v is the wave speed, ρ is the blood density, and A_c stands for the cross-sectionl area of the boundary at the OV.

2.5.2 Mathematical implementation

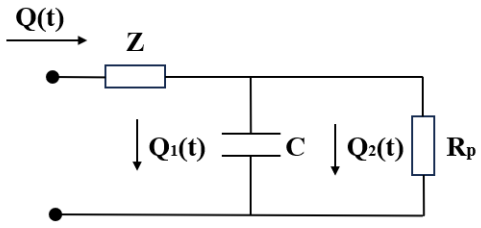

Figure 8: 3-element Windkessel model circuit.

According to the electrical analogy, flow corresponds to electric current, distensibility is equivalent to capacitance, and flow resistance corresponds to electrical resistance/impedance. Since the 3-element WK model is a two-mesh circuit, applying Kirchhoff's current law to analyze it yields to equation 7.

$$Q(t) = Q_1(t) + Q_2(t) = C \cdot \frac{d[P(t) - Z \cdot Q(t)]}{dt} + \frac{P(t) - Z \cdot Q(t)}{R_p} \tag{7}$$

If Equation 7 is rearranged to leave the flow on the left side and the pressure on the right, Equation 8 is obtained. Having the two variables separately, the Laplace transform is applied (see Equation 9), and the transfer function is achieved, which is defined by Equation 10.

$$Q(t)\left(1 + \frac{Z}{R_p}\right) + C \cdot Z\left(\frac{dQ(t)}{dt}\right) = C\left(\frac{dP(t)}{dt}\right) + \frac{P(t)}{R_p} \tag{8}$$

$$Q(s)\left(1 + \frac{Z}{R_p} + CZs\right) = P(s)\left(Cs + \frac{1}{R_p}\right) \tag{9}$$

$$H(s) = \frac{P(s)}{Q(s)} = \frac{1 + \frac{Z}{R_p} + CZs}{Cs + \frac{1}{R_p}} \tag{10}$$

By implementing Equation 10 in *MATLAB*, pressure can be obtained by inputting the WK parameters and the flow rate.

2.5.3 Parameter estimation

Since the parameters of the WK model depend on vascular structure and distribution, they are specific to each patient. Impedance (Z) is calculated using patient-specific parameters obtained from ultrasound scans and reported in the patient's medical record. However, peripheral resistance (R_p) and distensibility (C) are more complex to determine, as they depend on a very extensive analysis of the vasculature that makes up the AVF, and on details that are not captured by arm MRIs.

Hence, to obtain the final values, a process of iteration took place until R_p and C values that made sense with the physiological data obtained from each patient were achieved. Because there is no real target pressure curve to optimize the estimated pressure through a cost function, the parameters to iterate were chosen in a usual range of values observed in articles: from $2 \cdot 10^7$ to $5 \cdot 10^{10}$ Pa·s/m^3 for the R_p, and $1 \cdot 10^{-12}$ to $1 \cdot 10^{-8}$ m^3/Pa for the C [58][21][11][13]. To choose the ideal combination of R_p and C, we determined that the pressure in the AVF should be between 70 - 80% of mean arterial pressure. In the case of patients with normotension (mean systolic pressure $<$ 140 mmHg and mean diastolic pressure $<$ 90 mmHg) the AVF pressure limit was given by the range of mean AVF pressure of 50 - 80 mmHg, while in hypertensive patients, this was given by 70 - 130 mmHg [59]. These ranges are not empirical and were approximated with the assistance of nephrologist Dr. Ibeas.

3 Results

Results are presented here for patients 1, 6 and 8. CFD simulations for the others are still in progress.

3.1 Mesh convergence study

Residual type	Δx = 0.69 mm	Δx = 0.63 mm	Δx = 0.51 mm	Δx = 0.25 mm
Continuity	0.05	0.05	0.55	0.85
X-velocity	0.0005	0.0005	0.0025	0.002
Y-velocity	0.0005	0.0005	0.0025	0.002
Z-velocity	0.0005	0.0005	0.0025	0.002

Table 5: Change in residual values according to each volume mesh density.

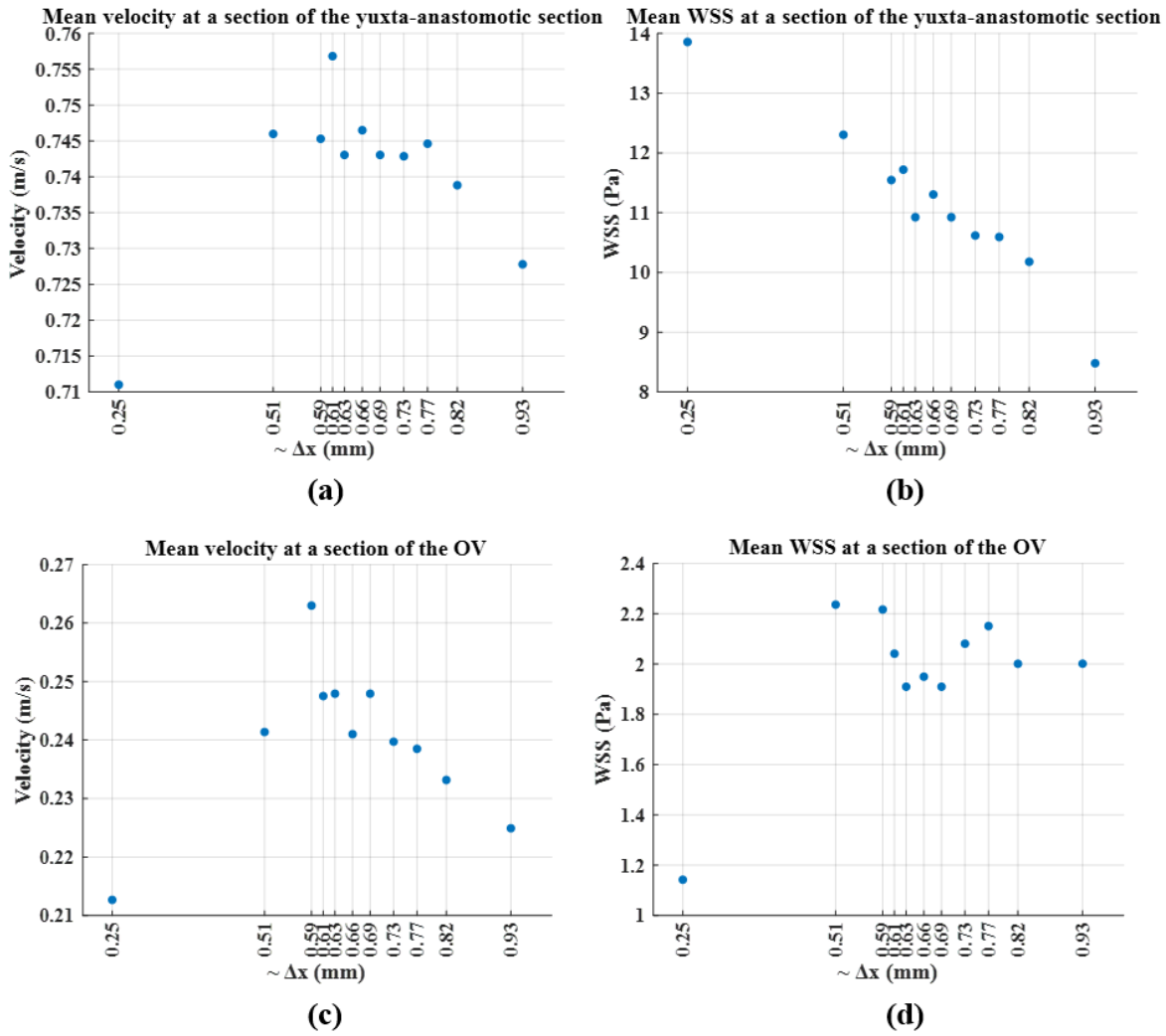

Figure 9: Average velocity and WSS results of the mesh convergence study for different mesh densities (i.e., Δx) in the outflow vein and yuxtaanastomotic zones. The exact area that was analyzed can be seen in the Appendix A.

If we focus on an analysis at the numerical level, as the mesh density increases (i.e., Δx decreases), there is no stabilization in the results (see Figure 9). This is also true for the analysis performed on the BCs, which can be found in the Appendix A. Qualitatively, changes are also observed in the visual distribution of the WSS in the different meshes. There is greater magnitude of WSS represented in the juxta-anastomotic zone in the 740k ($\Delta x = 0.51$ mm) and 6M-element ($\Delta x = 0.25$ mm) grids, which is the zone of greatest representation of WSS on the AVF for all meshes. This change in the representation of the WSS is accompanied by a significant change in the values of the residuals. For simplicity, only representative meshes from the convergence study are included in Table 5, since the intermediate values of residuals are not significant. Starting at the 390k volume mesh ($\Delta x = 0.63$ mm), there is an inflection point at which the residual values rise to more than 10^{-3}, which commonly is the threshold value for convergence [60].

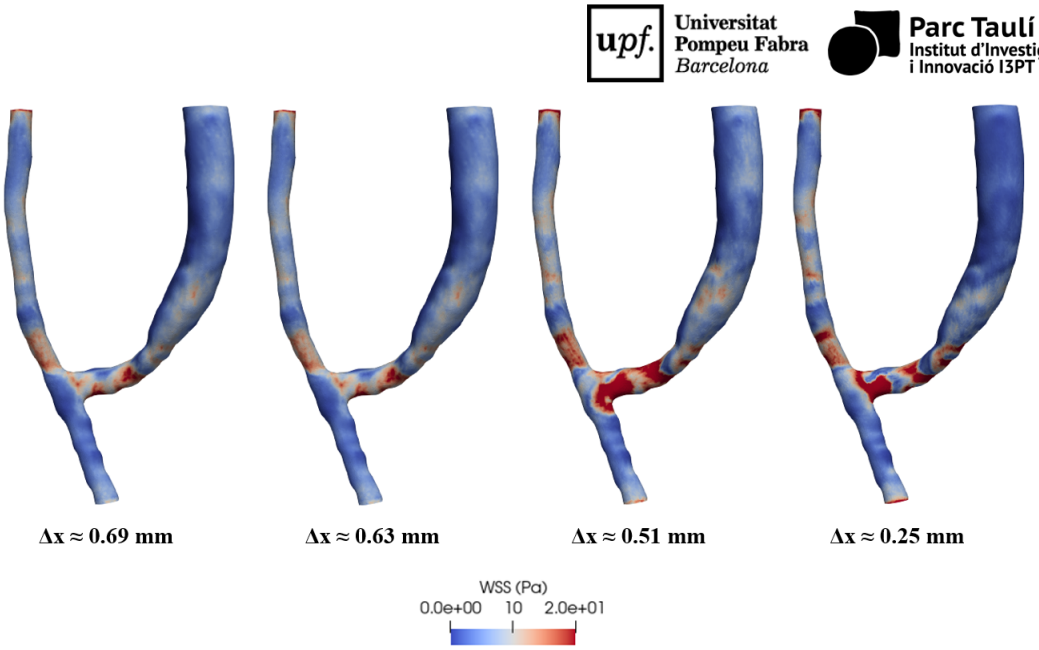

Figure 10: Morphological distribution of WSS for different mesh densities representative of the mesh convergence study.

3.2 Time step convergence study

Only two time steps meet the CFL condition: 1×10^{-4} sec and 5×10^{-4} sec. For the latter, *Fluent* utilized 4 cores for parallel processing when executed locally, resulting in a simulation time of $\sim$ 36 hours. For the 1×10^{-4} sec time step the computational time increased up to 10 hours more.

Δt(sec)	C
1×10^{-4}	0.1847
5×10^{-4}	0.9234
1×10^{-3}	1.8467
5×10^{-3}	9.2336
1×10^{-2}	18.4671
5×10^{-2}	92.3356

Table 6: Time step convergence study results according to the CFL condition.

3.3 Results from the 3-element Windkessel model

Table 7 specifies the parameters used to derive the pressure waveform for the OV outlet. An example for Patient 6, 6 months is seen in Figure 11. The fact that the contribution of the PA and DA to the OV flux is 75% and 25%, respectively can be observed in terms of magnitude in the velocity plot. Patient 6 has normotension (mean arterial pressure of 87.9 mmHg), and a mean pressure in the AVF corresponding to 70% of this.

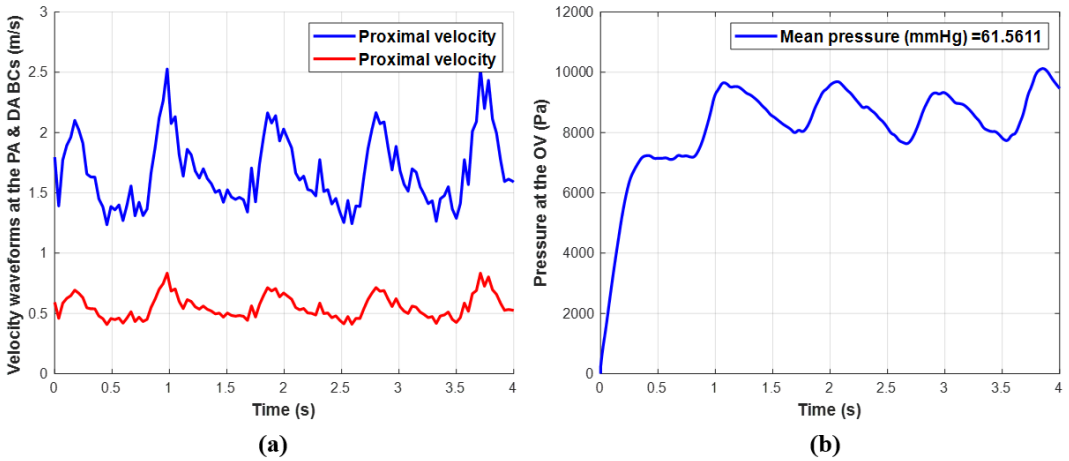

Figure 11: Data from Patient 6, 6 months. **(a)** Velocity waveforms for the proximal (PA) and distal (DA) segments of the artery, which are inlet BCs, and also inputs for the WK, as they are used to compute the flow. **(b)** Outlet pressure wavefrom in the outflow vein resulting from the WK model.

ID	Time period	Z (Kg/s·m^4)	Rp (Pa·s/m^3)	C (m^3/Pa)
Patient 1	1 week	9.82×10^7	5×10^8	1×10^{-10}
	1 month	5.31×10^7	5×10^8	5×10^{-10}
	6 months	5.17×10^7	1×10^8	5×10^{-9}
Patient 2	1 week	1.26×10^8	1×10^{10}	2×10^{-9}
	1month	4.63×10^7	2×10^8	1×10^{-11}
	6 months	4.16×10^7	1×10^8	1×10^{-11}
Patient 3	1 week	7.60×10^7	5×10^9	2×10^{-9}
	1month	6.44×10^7	1×10^9	1×10^{-9}
	6 months	7.62×10^7	1×10^9	1×10^{-9}
Patient 6	1 week	2.82×10^7	2×10^7	5×10^{-10}
	1month	2.27×10^7	5×10^7	5×10^{-10}
	6 months	1.57×10^7	5×10^8	1×10^{-10}
Patient 8	1 week	7.77×10^7	5×10^{10}	5×10^{-9}
	1month	4.92×10^7	1×10^{10}	1×10^{-8}
	6 months	NA	NA	NA
Patient 9	1 week	7.89×10^7	1×10^9	1×10^{-11}
	1month	9.35×10^7	1×10^9	5×10^{-12}

Table 7: 3-element Windkessel estimated model parameters. 'NA' stands for 'Not Available', meaning that the ultrasound for BC extraction for that time period in that particular patient was not available.

3.4 Temporal follow-up simulations: identified patterns

Case	WSS (Pa)		Pressure (Pa)		$\bar{V}$ (m/s)	
	YAS	OV	YAS	OV	YAS	OV
Patient 1, 1 week	22.10	11.17	44,932.96	44,050.57	1.04	0.91
Patient 1, 1 month	10.68	6.94	142,974.10	142,612.30	0.72	0.67
Patient 1, 6 months	10.36	7.28	143,037.80	142,668.20	0.71	0.66
Patient 6, 1 week	38.89	20.83	8,318.90	4,856.72	3.68	1.35
Patient 6, 1 month	26.24	16.10	2,470.87	3,513.66	1.49	0.75
Patient 6, 6 months	27.91	16.20	2,610.11	3,506.03	1.56	0.76
Patient 8, 1 week	8.88	4.18	7,593.29	7,933.29	0.42	0.45
Patient 8, 1 month	10.18	11.63	1,638.44	1,897.18	0.45	0.47
Patient 8, 6 months	18.26	12.11	14,493.87	15,200.93	0.80	1.03

Table 8: Physical parameters of the AVF for different patients (1, 6 and 8). 'YAS' stands for 'yuxtaanastomotic' and 'OV' for 'outflow vein'.

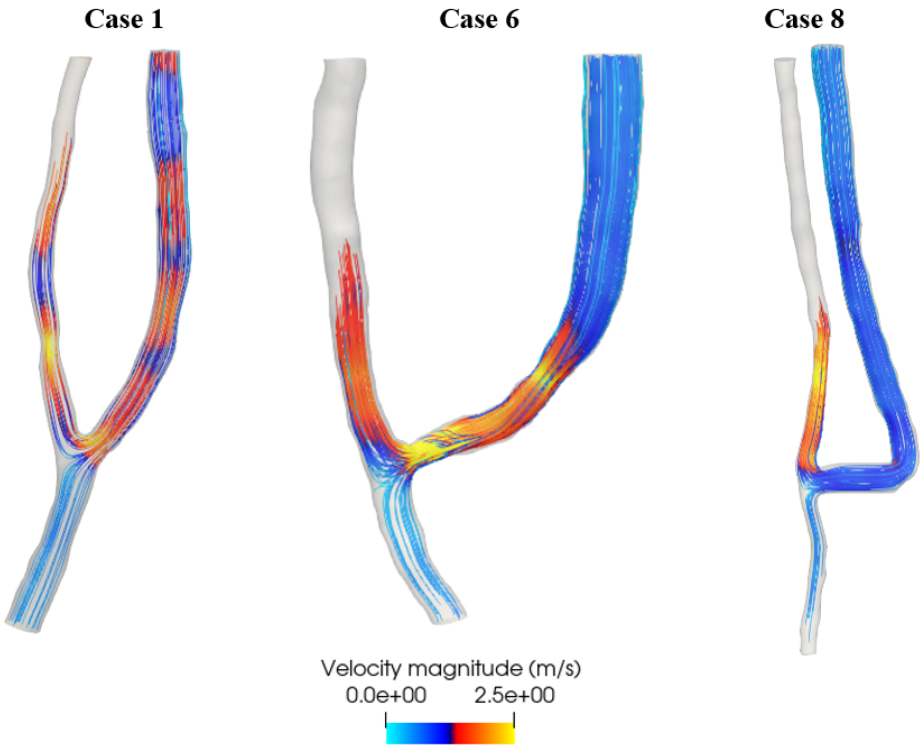

Figure 12: Velocity pathlines in the different geometries for one week. The pathline pattern is repeated for one month and six months.

ID	Time period	$Re_{outflowvein}$	$Re_{yuxta-anastomosis}$
Patient 1	1 week	32.25	40.28
	1month	23.70	26.45
	6 months	25.70	28.38
Patient 6	1 week	74.04	212.68
	1month	27.33	32.35
	6 months	26.99	34.73
Patient 8	1 week	12.94	15.57
	1month	19.38	30.08
	6 months	42.17	45.69

Table 9: Mean Reynolds number (Re) in the outflow vein and juxta-anastomotic zones.

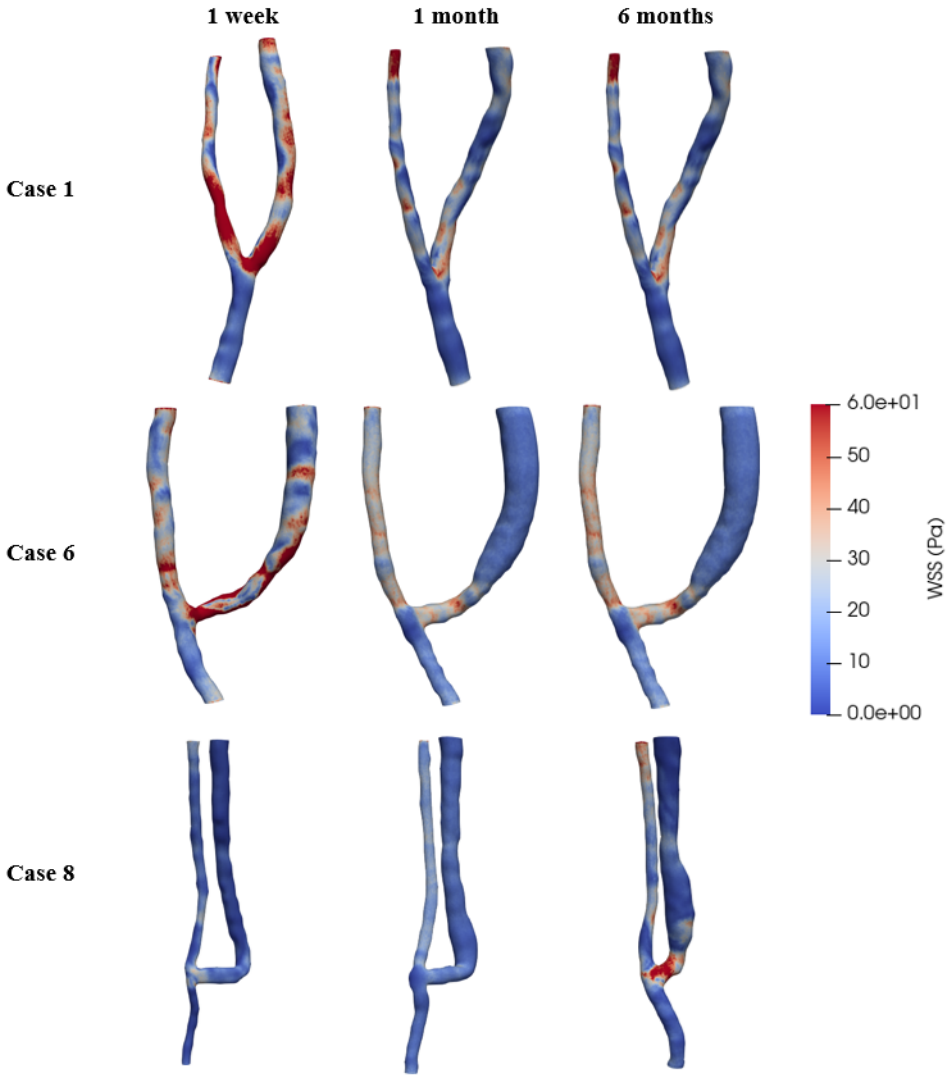

Figure 13: Temporal evolution of WSS distribution in the different AVFs.

In this section, the temporal evolution of the AVF is presented using physical parameters, such as the WSS (see Table 8). At the visual level, the path of blood through the AVF is observed in Figure 12. The greatest magnitude of velocity is located in the juxta-anastomotic zone, with a lesser magnitude in the case of patient 8. The flow pathlines are laminar (i.e., Re $<$ 2,000) (see Figure 12 and Table 9). The areas where there is a higher velocity usually coincide with a higher WSS magnitude (see Figure 13).

3.5 Morphological parameters from arteriovenous fistulas segmentations

ID	Time period	$D_{outflowvein}$ (mm)	$D_{anastomosis}$ (mm)	AVF angle (°)
Patient 1	1 week	4.81	5.28	36.12
	1month	6.54	7.38	37.03
	6 months	6.63	7.41	41.00
Patient 2	1 week	4.25	4.01	64.99
	1month	7.01	6.22	65.01
	6 months	7.39	5.56	68.73
Patient 3	1 week	5.47	4.78	52.86
	1month	5.94	4.79	54.42
	6 months	5.46	3.59	42.47
Patient 4	1 week	5.96	4.52	89.88
	1month	6.83	3.88	73.11
	6 months	7.63	5.09	24.63
Patient 5	1 week	4.22	4.50	44.20
	1month	4.31	3.79	44.32
	6 months	4.82	4.71	31.56
Patient 6	1 week	8.97	4.91	77.89
	1month	10.01	6.99	79.67
	6 months	12.05	7.84	83.22
Patient 7	1 week	5.41	7.83	8.45
	1month	6.80	6.05	8.54
	6 months	8.06	5.94	9.33
Patient 8	1 week	5.41	4.58	35.44
	1month	6.80	5.11	33.53
	6 months	8.06	6.21	25.67
Patient 9	1 week	5.37	5.07	90
	1month	4.93	5.19	106.73
	6 months	7.05	5.44	42.86

Table 10: Morphological data from all the AVFs segmented in the study. The diameter of the anastomosis refers to the diameter at the binding site.

Table 10 includes morphological parameters from the AVF structure for all patients, including the anastomosis angle (between the artery and the OV), the diameter for the outflow vein BC, as well as the anastomosis diameter at the binding site.

4 Discussion

4.1 Mesh convergence study

The mean WSS values calculated for the different mesh densities in the juxta-anastomotic section range from 4 to 14 Pa (see Figure 9). Considering that this zone is most commonly affected by flow and has the highest mean velocity magnitude, these results are consistent with the literature in all cases. Literature commonly reports WSS values ranging from 9 to 20 Pa for this zone and 1.5 to 9 Pa for the remaining zones [14][61]. In the most proximal zone of the OV, the WSS ranges between 1.1 Pa and 2.25 Pa, which is reasonable considering that it is a zone where the flow starts to stabilize. The pressure values may be underestimated compared to what is usually seen in the literature. In the juxta-anastomotic zone, the pressures do not reach 100 Pa, and in the OV, they do not reach 10 Pa. Literature often reports values higher than 10,000 Pa [61]. However, pressure estimation through CFD is one of the most variable parameters in the literature. Regarding velocity, in the juxta-anastomotic zone, it has a higher magnitude, ranging from 0.7 to 0.8 m/s, while in the OV, it ranges from 0.2 to 0.3 m/s. This is consistent with the clinical picture of patients with AVFs.

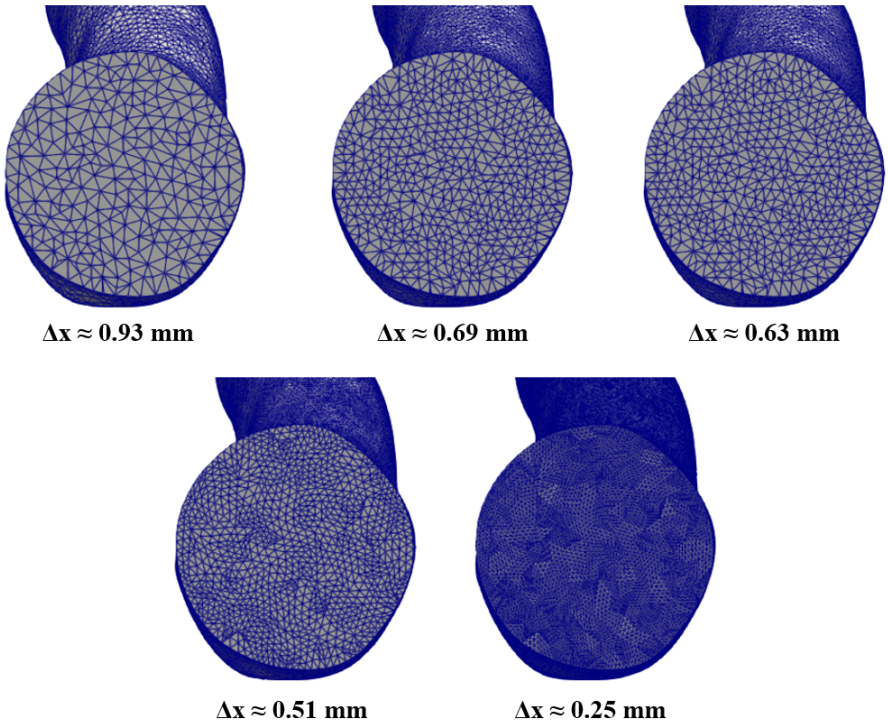

Figure 14: Element distribution for several mesh densities.

Due to the lack of clear stabilization indicating a mesh-independent state of the results (neither in Figure 9 nor in Figures 17, 18, 19, 20, 21 of the Appendix A), and the increase in residual values from the 390k (i.e., $\Delta x = 0.63$ mm) mesh on, the volumetric density of 390k elements was chosen as the desired mesh density for the next steps of the workflow. This increase in residuals may be due to the quality of the mesh.

All volume meshes were constructed in *Gmsh*. Although the tetrahedra were optimized with filters, they are not quite regular at the boundaries and on the area of the bifurcation of the anastomosis. In addition, the meshes obtained with the "Split by 2" option (with densities of 740k (i.e., $\Delta x = 0.51$ mm) and 6M (i.e., $\Delta x = 0.25$ mm) volume elements) showed even more heterogeneous patterns. To improve this aspect, software that allows further mesh refinement would be needed. This refinement should also be done locally, implementing mesh grading [62], especially to increase the element density in the area of the artery-vein bifurcation, where significant flow gradients or complex flow characteristics are expected. Another option could be the combination of tetrahedra and hexahedra, as hexahedrons tend to exhibit better mesh quality metrics than tetrahedral elements [63]. They have lower aspect ratios, fewer highly skewed elements, and better shape regularity, which overall help to minimize numerical oscillations and ensure smoother convergence.

Nonetheless, achieving convergence in steady mode can be more challenging than in transient mode, primarily due to the interdependence of the iterations. In transient simulations, the solution evolves over time, with each time step advancing independently. In contrast, steady mode iterations are highly interdependent as the solution is obtained by iteratively solving the governing equations, utilizing the solution from the previous iteration as an initial guess, until a convergence criterion is satisfied. This interdependence means that changes in one part of the domain can affect other parts, leading to a prolonged convergence process that can be more difficult to achieve [64]. This difference in convergence complexity between steady and transient simulations may also explain the variation in residual values observed between steady and transient simulations. All of the transient simulations had residual values <0.001, while the steady ones were above this value. Therefore, it can be concluded that the steady mode is not a suitable approach for analyzing the hemodynamics of AVFs due to limitations with the allowable error in the simulations.

4.2 Time step convergence study

Using a smaller Courant number often requires smaller time steps, resulting in increased computational time and higher memory requirements due to the storage of more data points per simulation. Additionally, employing a smaller Courant number can cause the damping of certain features in the simulated solution, potentially leading to the loss of information when reproducing fast flow dynamics or sharp gradients [65]. Consequently, a time step of 5×10^{-4} sec was chosen instead of 1×10^{-4} sec.

4.3 Indentified patterns from the temporal follow-up

In all the analyzed cases (patient 1, patient 6, and patient 8), a distribution of WSS very similar to that presented in the literature is observed, with a greater presence of WSS in the juxta-anastomotic zone [11][14][2]. However, in patient 8, the magnitude of the velocities is higher upstream of the anastomotic zone, and not so much in the juxta-anastomotic zone. In patients 1 and 6, a higher magnitude of WSS is observed in the first week compared to the following two time periods, both in the juxta-anastomotic zone and the outflow vein. However, the opposite trend is seen in patient 8. This difference may be related to the juxta-anastomotic flexion of the vein, and the tendency towards higher WSS in the first weeks may be attributed to vascular adaptation to non-physiological flow. The WSS values are higher at the beginning of the anastomosis than in the proximal vein, which makes sense considering the collision of two flows in the same plane.

The mean pressure in both the juxta-anastomotic zone and the vein is higher in the first and sixth month compared to the first week for patients 1 and 8, but the opposite trend is observed in patient 6. Therefore, no clear temporal pattern regarding the pressure trend can be established. However, it can be deduced that there is an overestimation of pressure in the case of patient 1. When converted to mmHg to compare with the systolic blood pressure (120 mmHg) and diastolic blood pressure (80 mmHg) in the brachial artery of a healthy adult, the pressure values in the juxta-anastomotic area and the outflow vein range from ∼330 mmHg (∼45,000 Pa) to almost 1100 mmHg (∼143,000 Pa), which does not align with typical values found in the vascular system, even considering the artificial nature of the structure. The pressure values for patients 6 and 8 in both zones are more consistent, ranging between ∼20 - 60 mmHg (∼2,600 - 8,000 Pa) for patient 6 and ∼60 - 110 mmHg (∼7,600 - 14,500 Pa) for patient 8, who has hypertension.

Regarding velocity magnitudes, they are consistently higher in the juxta-anastomotic zone than in the vein zone, likely because the flow has already stabilized in the latter. In neither of the sections are turbulent flows observed, although it is true that the Reynolds number is higher in the juxta-anastomosis. It may be that turbulence occurs later in the OV, after passing the anastomosis, or that the description of the flow needs to be modified. A higher magnitude of velocity usually coincides with a higher magnitude or distribution of WSS. The highest velocity values are observed in patient 6, who also has the largest diameter in the outflow vein and at the binding site of the anastomosis. These velocities are twice as high as those observed in the other patients, indicating a direct proportionality between the diameter (i.e., the cross-sectional area, A_c) and velocity (v), and in turn, between these two parameters and flow. This demonstrates that the flow equation ($Q = v \cdot A_c$) is upheld, as patient 6 has twice the flow compared to the other patients.

The number of parameters to be analyzed could be extended to obtain more information on the effect of flow on the AVF evolution in terms of physiopathology, hemodynamics, and morphology.

4.4 Morphological parameters correlated with arteriovenous fistula hemodynamics

In all patients, the diameter of the outflow vein (OV) consistently displayed a gradual outward geometric expansion over time (see Table 10). This indicates the completion of the arterialization process. The observed flow values in Table 3, ranging between 850 - 2,200 mL/min, are in line with this finding. These flow rates signify a good capacity to accommodate hemodialysis (HD) treatment, considering that a minimum flow of 500 mL/min is required for successful HD. There is also no presence of stenosis in neither of them, which may hinder such treatment.

Furthermore, the diameter of the venous segment at the OV's proximal level has been found to be associated with AVF failure. An optimal diameter of the feeding vein and the flow is also related to predisposition for effective HD treatment. In this case, the conjecture holds true. Among the three patients, patient 6 exhibits the largest outflow vein diameter, increasing from 8.79 mm one week after the operation to 12.05 mm six months after. This patient also has the highest fistula flow, reaching 2,200 mL/min, which is twice as much as the others. Patient 1, with a diameter increase from 4.81 mm to 6.63 mm in half a year, achieves a flow of up to 1,200 mL/min, while patient 8, with a larger diameter ranging from 5.41 mm in the first week to 8.06 mm at six months, achieves a flow of up to 900 mL/min. Therefore, a larger diameter does not always directly correlate with a higher flow. More cases should be analyzed in order to draw solid conclusions in this regard. It is important to note that hypertension does not seem to affect the flow in patient 8, as it is the lowest among the three patients.

Since juxta-anastomotic stenosis is considered one of the primary factors associated with AVF failure, it can be excluded as a significant parameter in this study. In these cases, failure is typically caused by flow restriction and increased WSS resulting from a smaller diameter in the juxta-anastomotic area. However, it is worth noting that flow rates on the order of 2,000 mL/min can still be observed in the presence of 80% stenosis. Therefore, narrowing of this magnitude should undoubtedly be evaluated in forthcoming studies, as none of the patients in this research exhibited such a level of stenosis. This would also enable the assessment of the suitability of CFD models in mimicking AVF hemodynamics of patients who have a high level of stenosis but maintain good flow rates.

What is certainly observed in all three patients, however, is a widening of the diameter at the anastomotic site over time. Patient 1's diameter increased from 5.20 mm to 7.41 mm, patient 6's diameter increased from 4.91 mm to 7.84 mm, and patient 8's diameter increased from 4.58 mm to 6.21 mm, all in six months time. This widening may be attributed to the high velocities experienced in the juxta-anastomotic zone, where flow from the distal and proximal artery converges. The greater distribution of WSS in this area could potentially lead to modifications in the AVF's walls, resulting in an increase in the local vessel diameter. Interestingly, this increase in diameter does not appear to be correlated with AVF failure.

Another indicator of AVF failure that has been considered previously is the degree of tortuosity or curvature along the AVF pathway, which has been associated with increased risk of AVF failure [30]. Indeed, obtuse angles have shown a tendency to exhibit reduced WSS in previous CFD studies [36], suggesting a potential decrease in the occurrence of AVF failures. In the cases of patient 1 and patient 6, there is a slight increase in the artery-vein angle over time. Patient 1's angle increases from 36.12° to 41.00°, while patient 6's angle increases from 77.89° to 83.22°. Both patients exhibit an AVF with a well-defined angle and lack abrupt curves that would give it a 'U'-shape. On the other hand, patient 8's AVF displays a junction that results in a tortuous angle, with significant bending of the vein (see Figure 6), particularly during the first week (35.44°) and first month (25.67°). However, by the sixth month, this flexion almost disappears, resulting in an angle of 25.67°, smaller than the previous measurements for this geometry. Because of this change, the WSS is ditributed in the juxta-anastomotic zone. Therefore, the morphology of the AVF and how the anastomosis is made plays an important role in the hemodynamic pressure on the vascular structure. From the clinical characterization of patient 8's AVF (no stenosis or insufficient flow), it cannot be definitively concluded that the tortuosity caused by the nearly 90° flexion of the vein with respect to the artery is directly related to AVF failure. Nonetheless, it is worth noting that patient 8 exhibits the lowest flow rate among the three patients. It is believed that higher levels of tortuosity can disrupt laminar flow, promote turbulence, and increase the likelihood of thrombus formation and stenosis.

Lastly, the depth and anatomical location of the AVF have also been hypothesized to be related to AVF pathophysiology. In this study, each patient has a different type of AVF junction: patient 1 has a radial-perforating AVF, patient 6 has a brachiocephalic AVF, and patient 9 has a brachial-perforating AVF. However, since the sample size is limited and diverse AVF types are not well-represented, clear conclusions cannot be drawn regarding this aspect [7].

4.5 Limitations and future work

4.5.1 Raw data

An initial limitation was the presence of blurriness in certain areas of the MRIs, making it challenging to discern structures clearly. This blurriness is likely attributed to slight movements during the image acquisition process. Overcoming this issue would require the establishment of a standardized protocol to maintain image quality. The blurriness might have affected the segmentation of the AVF, potentially compromising the accuracy of its morphological measurements. Furthermore, one way to optimize the presented workflow in terms of time and accuracy would be the use of automatic segmentation using region-based or edge detection methods. This improvement would also benefit from an image acquisition protocol.

In the case of ultrasound scans performed on patients, these scans are conducted by placing the Doppler ultrasound probe in specific locations where flow is to be

checked, such as the inflow artery, the outflow vein, or the AVF site. To obtain the flow values, the vessel diameter must be manually entered into the ultrasound machine, which can introduce errors. Additionally, the flow waveforms are obtained by keeping the probe fixed on the patient's arm and waiting a few seconds for the flow to stabilize on the screen before considering it reliable. Consequently, this process heavily relies on the skill and experience of the physician who extracts the data.

4.5.2 Towards an enhanced computational model

The implemented BCs so far consist of time-dependent velocity or pressure profiles. These BCs aim to approximate the temporal behavior and mimic pulsatility of the flow. However, they do not provide a spatial description of the flow, as would be achieved with Hagen-Poiseuille type parabolic velocity profiles [66]. The parabolic shape of the velocity profile emerges due to the balance between viscous shear forces and pressure-driven flow in laminar conditions. Additionally, since parabolic profiles incorporate flow development, they are theoretically less influenced by entry or exit effects in the vessels. As a result, parabolic velocity profiles generally offer greater stability and are less prone to numerical instabilities during simulations. This reduces the likelihood of encountering convergence issues or oscillations in the solution.

It has been described that turbulent flow should occur near the anastomosis due to the contribution of flow from the distal and proximal sites, a phenomenon that can extend up to the posterior 5 cm [7]. However, parts distant to the anastomosis tend to have laminar flow. Mixed turbulent/laminar flow behavior models are employed to simulate this coexistance, and could help to better capture the flow behavior in the AVF. In CFD, two primary approaches are used to model mixed flow behavior: Reynolds-averaged Navier-Stokes (RANS) modeling and Large Eddy Simulation (LES). While primarily approximating turbulent fluctuations through the Reynolds stress, RANS modeling is still capable of capturing the diverse behaviors exhibited by laminar, transitional, and turbulent flows, although with certain limitations [67]. LES is as a more accurate alternative mathematical model for turbulence than RANS. Its approach involves directly resolving the larger and more influential eddies that contribute to flow dynamics, while employing subgrid-scale (SGS) models to represent the smaller, dissipative eddies [68]. This capability enables the examination of intricate flow phenomena, including flow separation and shear layers. Since in the case of AVF turbulent phenomena occur locally (in the juxta-anastomotic zone), this model could be suitable to have a better description of the flow in these zones.

Boundary layers are fluid regions that develop along solid boundaries, where the velocity equation undergoes a variation: starting from zero at the boundary due to the no-slip condition, and gradually reaching a value that is mostly unaffected by the proximity of the boundary, determined by the prevailing flow conditions [69]. Probably because of the bifurcation at the junction of the vein to the artery at the anastomosis, the normal vectors of these structures overlap. This produced errors when extruding the geometry to generate the boundary layers in *Ansys Fluent*, as

well as when trying other methods as the offset method. This error should be corrected to reduce the error in the results.

Since it is an arterialized vascular system, the walls of the AVF have compliance in real conditions. This is omitted from the model as a simplification. To provide a higher degree of realism, mechanical motion should be incorporated into the AVF vessels using a Fluid-Structure Interaction (FSI) model. Since stenosis in the juxta-anastomotic area is usually caused by the onset of neointimal hyperplasia (NH), different vessel wall thicknesses should be modeled to better reflect how the lumen of the vessel through which blood passes changes.

The WK model is 0-dimensional, since it considers the flow and pressure distribution in the vascular system to be uniform. Thus, the study of flow distribution and local changes in flow will be limited. Despite this, it still represents the most suitable model for arterial-type flow in an outlet BC, especially since pressure at the outflow vein cannot be easily obtained *in-vivo*, as in the case of AVF since it would be too invasive for the patients. However, in the event that a cuff could be positioned in the vein to measure pressure during the surgical procedure, the simulated output from the 3-element Windkessel model should be adjusted to fit the measured data using a cost function. This could serve as validation with the aim of obtaining the most realistic output achievable, ultimately striving for proper correlation coefficients. Another prospective undertaking would involve conducting a sensitivity analysis to assess the impact of individual model parameters on the overall performance of the model. Technically, the incorporation of the 3-element WK model into the *Ansys Fluent* solver would indeed be advantageous. The extension 'Winkessel v3' [70] presents compatibility issues with the existing user-defined function (UDF) library when attempting to adapt it to newer versions, since it was designed for *Fluent* 17.0, 17.1, or 17.2.

4.5.3 Towards clinical applications

Although this model has the short-term goal of better understanding fistula pathophysiology over time, there are similar CFD-based tools that provide clinical diagnostic support for clinicians, and are actually being commercialized. An example of this is *HeartFlow* [71], a company specializing in cardiovascular diagnostics for coronary artery disease, which received FDA-granted clearance in 2014 for its use in clinical practice. Particularly, the company's key product is the '*HeartFlow* FFRct Analysis', a non-invasive diagnostic tool designed to assess the severity of coronary artery blockages. By combining computed tomography (CT) imaging, CFD, and advanced algorithms, it creates a 3D model of a patient's coronary arteries and analyzes blood flow dynamics. Through an index known as fractional flow reserve (FFR), the *HeartFlow* tool provides a comprehensive evaluation of the functional significance of coronary artery blockages, without the need for invasive procedures like cardiac catheterization to determine the most suitable treatment course. Given the similarities between AVF failure and coronary artery blockage, a similar index could be used to quickly determine whether an AVF should be re-operated or as a prevention tool for low-flow AVFs that require more frequent monitoring.

Moreover, if the number of study cases were to increase to include a sufficiently large cohort, it would be possible to draw conclusions that could be extrapolated to a standard group of real patients. This would enable the firm determination of correlated morphological patterns related to AVF failure. In such scenarios, CFD simulations could be utilized to predict geometries associated with AVF failure. A similar approach to that of *HeartFlow* could be adopted to generate these predictions. This approach would facilitate a more strategic and targeted utilization of implanted blood vessel support devices [72]. These devices, composed of biocompatible materials, are surgically implanted either during the initial AVF creation or in a subsequent procedure. Their primary purpose is to offer structural support and stabilization to AVFs, aiming to prevent complications such as stenosis, aneurysm formation, or vessel collapse. By employing a predictive model, the use of these devices could be guided to mitigate risk factors. Such an approach would aid in preserving the patency and functionality of the AVF, thus ensuring optimal blood flow for efficient dialysis.

5 Conclusion

The present study involves nine patient cases, out of which three complete *in-silico* simulations have been conducted, while the already prepared ones are still in progress. One of the primary objectives of this study has been to evaluate the temporal evolution of the AVF to identify critical time periods in its development and correlate them with morphological parameters. By gaining insights into these critical stages, closer monitoring of the AVF could be achieved if the model is further improved, facilitating better patient care. Moreover, this study incorporates previously unconsidered clinical parameters, such as the patient's state of normotension or hypertension, thus enhancing the model's suitability in representing patient hemodynamics. To advance further in this direction, efforts should be directed towards optimizing the model to better capture the flow behavior in complex areas, such as the bifurcation of the anastomosis. Additionally, exploring new mathematical models for flow description and enhancing the definition of the boundary conditions are crucial aspects that need to be addressed. It is also essential to expand the scope of case studies by increasing their number.

These novel aspects pave the way for the computational model presented in this thesis to serve as the foundation for developing accurate and realistic patient-specific CFD simulations. This approach surpasses the current state of the art in the literature by providing a more personalized perspective to numerical models attempting to describe scenarios within the human body in patients with end-stage renal disease.

References

[1] Csaba P Kovesdy. "Epidemiology of chronic kidney disease: an update 2022". In: *Kidney International Supplements* 12.1 (2022), pp. 7–11.

[2] TJ Barber et al. "The fluid dynamics of arterio-venous fistulae and the clinical relevance". In: (2018).

[3] *File:Hemodialysis-en.svg - Wikimedia Commons — commons.wikimedia.org*. https://commons.wikimedia.org/wiki/File:Hemodialysis-en.svg#file. [Accessed 10-Jun-2023].

[4] "Esperando un Trasplante de Riñón - Guía para personas con Enfermedad Renal Crónica". In: (). Accessed: May 21, 2022.

[5] "NHS. (n.d.). Overview - Dialysis. NHS choices." In: (). Accessed: December 1, 2022.

[6] "Hemodialysis (no date) National Institute of Diabetes and Digestive and Kidney Diseases. U.S. Department of Health and Human Services." In: (). Accessed: June 23, 2022.

[7] José Ibeas et al. "Guıa clınica española del acceso vascular para hemodiálisis". In: *Nefrologıa* 37 (2017), pp. 1–191.

[8] *Types of Arteriovenous Fistulas — statpearls.com*. https://www.statpearls.com/articlelibrary/viewarticle/21793/. [Accessed 19-Jun-2023].

[9] *Department of Surgery - Vascular Access for Hemodialysis — surgery.ucsf.edu*. https://surgery.ucsf.edu/conditions--procedures/vascular-access-for-hemodialysis.aspx. [Accessed 10-Jun-2023].

[10] *Haemodialysis access with an arteriovenous fistula — kidneycareuk.org*. https://www.kidneycareuk.org/about-kidney-health/treatments/dialysis/haemodialysis-access-arteriovenous-fistula/. [Accessed 18-Jun-2023].

[11] George Hyde-Linaker et al. "Patient-specific computational haemodynamics associated with the surgical creation of an arteriovenous fistula". In: *Medical Engineering & Physics* 105 (2022), p. 103814.

[12] Yan-Ting Shiu et al. "Arteriovenous conduits for hemodialysis: how to better modulate the pathophysiological vascular response to optimize vascular access durability". In: *American Journal of Physiology-Renal Physiology* 316.5 (2019), F794–F806.

[13] AM de Villiers et al. "A validated patient-specific FSI model for vascular access in haemodialysis". In: *Biomechanics and modeling in mechanobiology* 17 (2018), pp. 479–497.

[14] Daniel M Jodko et al. "A two-stage model of an arteriovenous fistula maturation process". In: *Acta Bioeng. Biomech* 22 (2020), pp. 139–153.

[15] Muhammad A Siddiqui, Suhel Ashraff, and Thomas Carline. "Maturation of arteriovenous fistula: analysis of key factors". In: *Kidney research and clinical practice* 36.4 (2017), p. 318.

[16] Connor V Cunnane, Eoghan M Cunnane, and Michael T Walsh. "A review of the hemodynamic factors believed to contribute to vascular access dysfunction". In: *Cardiovascular engineering and technology* 8 (2017), pp. 280–294.

[17] Leonard D Browne et al. "The role of shear stress in arteriovenous fistula maturation and failure: a systematic review". In: *PloS one* 10.12 (2015), e0145795.

[18] Bogdan Ene-Iordache et al. "Disturbed flow in a patient-specific arteriovenous fistula for hemodialysis: multidirectional and reciprocating near-wall flow patterns". In: *Journal of biomechanics* 48.10 (2015), pp. 2195–2200.

[19] Monica Sigovan et al. "Vascular remodeling in autogenous arterio-venous fistulas by MRI and CFD". In: *Annals of biomedical engineering* 41 (2013), pp. 657–668.

[20] Yong He et al. "Serial analysis of lumen geometry and hemodynamics in human arteriovenous fistula for hemodialysis using magnetic resonance imaging and computational fluid dynamics". In: *Journal of biomechanics* 46.1 (2013), pp. 165–169.

[21] Patrick M McGah et al. "Effects of wall distensibility in hemodynamic simulations of an arteriovenous fistula". In: *Biomechanics and modeling in mechanobiology* 13.3 (2014), pp. 679–695.

[22] Radojica Stolic. "Most important chronic complications of arteriovenous fistulas for hemodialysis". In: *Medical principles and practice* 22.3 (2013), pp. 220–228.

[23] LC Bylsma et al. "Arteriovenous fistulae for haemodialysis: a systematic review and meta-analysis of efficacy and safety outcomes". In: *European journal of vascular and endovascular surgery* 54.4 (2017), pp. 513–522.

[24] "NKF Kdoqi Clinical Practice Guidelines. National Kidney Foundation". In: (). Accessed: October 12, 2022.

[25] Bogdan Ene-Iordache et al. "Computational fluid dynamics of a vascular access case for hemodialysis". In: *J. Biomech. Eng.* 123.3 (2001), pp. 284–292.

[26] Olivia Ng et al. "The effect of assumed boundary conditions on the accuracy of patient-specific CFD arteriovenous fistula model". In: *Computer Methods in Biomechanics and Biomedical Engineering: Imaging & Visualization* (2022), pp. 1–13.

[27] Neda Alam and David Newport. "Influence of Wall Compliance on the Flow Patterns in a Patient-Specific Brachio-Cephalic Arterio-Venous Fistula". In: *Biomechanics* 2.2 (2022), pp. 158–173.

[28] John E Carroll et al. "Tracking geometric and hemodynamic alterations of an arteriovenous fistula through patient-specific modelling". In: *Computer methods and programs in biomedicine* 186 (2020), p. 105203.

[29] Daniel Jodko et al. "Numerical investigations of the unsteady blood flow in the end-to-side arteriovenous fistula for hemodialysis". In: *Acta of bioengineering and biomechanics* 18.4 (2016), pp. 3–13.

[30] Jinkee Lee et al. "Assessing radiocephalic wrist arteriovenous fistulas of obtuse anastomosis using computational fluid dynamics and clinical application". In: *The Journal of Vascular Access* 17.6 (2016), pp. 512–520.

[31] Leonard D Browne et al. "In vivo validation of the in silico predicted pressure drop across an arteriovenous fistula". In: *Annals of biomedical engineering* 43 (2015), pp. 1275–1286.

[32] Leonard D Browne, Michael T Walsh, and Philip Griffin. "Experimental and numerical analysis of the bulk flow parameters within an arteriovenous fistula". In: *Cardiovascular engineering and technology* 6 (2015), pp. 450–462.

[33] N Lwin et al. "Experimental and computational analysis of a typical arteriovenous fistula". In: *19th Australasian Fluid Mechanics Conference (December, 2014)*. 2014.

[34] Iolanda Decorato et al. "Numerical simulation of the fluid structure interactions in a compliant patient-specific arteriovenous fistula". In: *International journal for numerical methods in biomedical engineering* 30.2 (2014), pp. 143–159.

[35] Bogdan Ene-Iordache and Andrea Remuzzi. "Disturbed flow in radial-cephalic arteriovenous fistulae for haemodialysis: low and oscillating shear stress locates the sites of stenosis". In: *Nephrology Dialysis Transplantation* 27.1 (2012), pp. 358–368.

[36] Bogdan Ene-Iordache et al. "Effect of anastomosis angle on the localization of disturbed flow in 'side-to-end'fistulae for haemodialysis access". In: *Nephrology Dialysis Transplantation* 28.4 (2013), pp. 997–1005.

[37] Zaher Kharboutly et al. "Numerical and experimental study of blood flow through a patient-specific arteriovenous fistula used for hemodialysis". In: *Medical engineering & physics* 32.2 (2010), pp. 111–118.

[38] A Ciandrini et al. "A CFD model of hemodynamics in hemodialysis vascular access". In: *Modelling in Medicine and Biology VI* 2 (2005), p. 341.

[39] Jeffrey E Hull et al. "Computational fluid dynamic evaluation of the side-to-side anastomosis for arteriovenous fistula". In: *Journal of vascular surgery* 58.1 (2013), pp. 187–193.

[40] *The Low Reynolds Number k-x3B5; Turbulence Model — doc.comsol.com*. https://doc.comsol.com/5.5/doc/com.comsol.help.cfd/cfd_ug_fluidflow_single.06.092.html. [Accessed 10-Jun-2023].

[41] Iolanda Decorato et al. "Numerical study of the influence of wall compliance on the haemodynamics in a patient-specific arteriovenous fistula". In: *Computer Methods in Biomechanics and Biomedical Engineering* 14.sup1 (2011), pp. 121–123.

[42] Bogdan Ene-Iordache and Andrea Remuzzi. "Blood flow in idealized vascular access for hemodialysis: a review of computational studies". In: *Cardiovascular engineering and technology* 8 (2017), pp. 295–312.

[43] Sanjiv Gunasekera et al. "Impact of juxta-anastomotic stent implantation on the haemodynamics within a single representative patient AVF". In: *International Journal of Heat and Fluid Flow* 92 (2021), p. 108874.

[44] Daniel Jodko et al. "Blood flows in end-to-end arteriovenous fistulas: Unsteady and steady state numerical investigations of three patient-specific cases". In: *Biocybernetics and Biomedical Engineering* 37.3 (2017), pp. 528–539.

[45] *SST k-omega model – CFD-Wiki, the free CFD reference — cfd-online.com*. https://www.cfd-online.com/Wiki/SST_k-omega_model. [Accessed 10-Jun-2023].

[46] *Simple Region Growing Segmentation x2014; 3D Slicer documentation*. https://slicer.readthedocs.io/en/latest/user_guide/modules/simpleregiongrowingsegmen
html. [Accessed 13-Jun-2023].

[47] Alexander Belyaev and Yutaka Ohtake. "A comparison of mesh smoothing methods". In: *Israel-Korea Bi-national conference on geometric modeling and computer graphics*. Vol. 2. Citeseer. 2003.

[48] https://www.gmsh.info/dev/doc/texinfo/gmsh.pdf.

[49] *Ansys Fluent 12.0 text command list - 6. mesh/*. https://www.afs.enea.it/project/neptunius/docs/fluent/html/tuilist/node7.htm.

[50] *Navier-Stokes Equations | Introduction to CFD — cfd.blogs.upv.es*. https://cfd.blogs.upv.es/introduction/navier-stokes-equations/. [Accessed 19-Jun-2023].

[51] Ehsan Khalili et al. "On The Importance of Fundamental Computational Fluid Dynamics Towards a Robust and Reliable Model of Left Atrial Flows: Is There More Than Meets the Eye?" In: *arXiv preprint arXiv:2302.01716* (2023).

[52] *Tips amp; Tricks: Convergence and Mesh Independence Study | Computational Fluid Dynamics (CFD) Blog x2013; LEAP Australia amp; New Zealand — computationalfluiddynamics.com.au*. https://www.computationalfluiddynamics.com.au/convergence-and-mesh-independent-study/. [Accessed 14-Jun-2023].

[53] Wassee Syed. *What is a Mesh Independence Study? - FEA Tips — featips.com*. https://featips.com/2019/03/31/what-is-a-mesh-independence-study/. [Accessed 14-Jun-2023].

[54] Guilherme Caminha. *The CFL Condition and How to Choose Your Timestep Size | SimScale — simscale.com*. https://www.simscale.com/blog/cfl-condition/. [Accessed 14-Jun-2023].

[55] *Courantx2013;Friedrichsx2013;Lewy condition – CFD-Wiki, the free CFD reference — cfd-online.com*. https://www.cfd-online.com/Wiki/Courant%E2%80%93Friedrichs%E2%80%93Lewy_condition. [Accessed 14-Jun-2023].

[56] Elie Nader et al. "Blood rheology: key parameters, impact on blood flow, role in sickle cell disease and effects of exercise". In: *Frontiers in physiology* 10 (2019), p. 1329.

[57] *Cardiovascular biomechanics, 6.2 Lumped models — folk.ntnu.no*. https://folk.ntnu.no/leifh/teaching/tkt4150/._main026.html. [Accessed 16-Jun-2023].

[58] Sulav Bastola and Steven A Jones. "Comparison of various zero-dimensional models to analyze the brachial artery blood flow of an arterio-venous fistula during hemodialysis procedure". In: *Engineering Reports* 3.10 (2021), e12403.

[59] CDC. *High Blood Pressure Symptoms, Causes, and Problems | cdc.gov — cdc.gov*. https://www.cdc.gov/bloodpressure/about.htm. [Accessed 16-Jun-2023].

[60] *Ansys Fluent 12.0 user's Guide - 26.18.1 judging convergence*. https://www.afs.enea.it/project/neptunius/docs/fluent/html/ug/node833.htm.

[61] Eamonn Colley et al. "A longitudinal study of the arterio-venous fistula maturation of a single patient over 15 weeks". In: *Biomechanics and Modeling in Mechanobiology* 21.4 (2022), pp. 1217–1232.

[62] *OpenFOAM v6 User Guide — doc.cfd.direct*. https://doc.cfd.direct/openfoam/user-guide-v6/blockmesh. [Accessed 19-Jun-2023].

[63] Teseo Schneider et al. "A large scale comparison of tetrahedral and hexahedral elements for finite element analysis". In: *ACM transactions on graphics* (2022).

[64] *How to Check Convergence of a CFD Simulation in SimScale? — simscale.com*. https://www.simscale.com/knowledge-base/how-to-check-convergence-of-a-cfd-simulation/. [Accessed 19-Jun-2023].

[65] *Breaking the Courant Number barrier for multiphase flow - Simcenter — blogs.sw.siemens.com*. https://blogs.sw.siemens.com/simcenter/multiphase-flow-cfd-and-courant-number/. [Accessed 19-Jun-2023].

[66] *Poiseuille Flow — thermopedia.com*. https://www.thermopedia.com/content/1042/. [Accessed 19-Jun-2023].

[67] *RANS | Introduction to CFD — cfd.blogs.upv.es*. https://cfd.blogs.upv.es/turbulence/rans/. [Accessed 19-Jun-2023].

[68] Michael Berk. *Large Eddy Simulations — towardsdatascience.com*. https://towardsdatascience.com/large-eddy-simulations-e485dd929682. [Accessed 19-Jun-2023].

[69] *What y+ should I use? Part 1 x2013; Understanding the physics of boundary layers | Computational Fluid Dynamics (CFD) Blog x2013; LEAP Australia amp; New Zealand — computationalfluiddynamics.com.au*. https://www.computationalfluiddynamics.com.au/y-plus_part1_understanding-the-physics-of-boundary-layers/. [Accessed 19-Jun-2023].

[70] *Ansys Store WindkesselV3 created by Ansys Inc — catalog.ansys.com*. https://catalog.ansys.com/product/5b3bc6857a2f9a5c90d32ee8/windkessel. [Accessed 19-Jun-2023].

[71] Heartflow. *Transforming the diagnosis and management of coronary artery disease*. https://www.heartflow.com/.

[72] Nikolaos Karydis et al. "An implanted blood vessel support device for arteriovenous fistulas: a randomized controlled trial". In: *American Journal of Kidney Diseases* 75.1 (2020), pp. 45–53.

A Appendix

Figure 15 shows all segmentations that have been performed for this thesis.

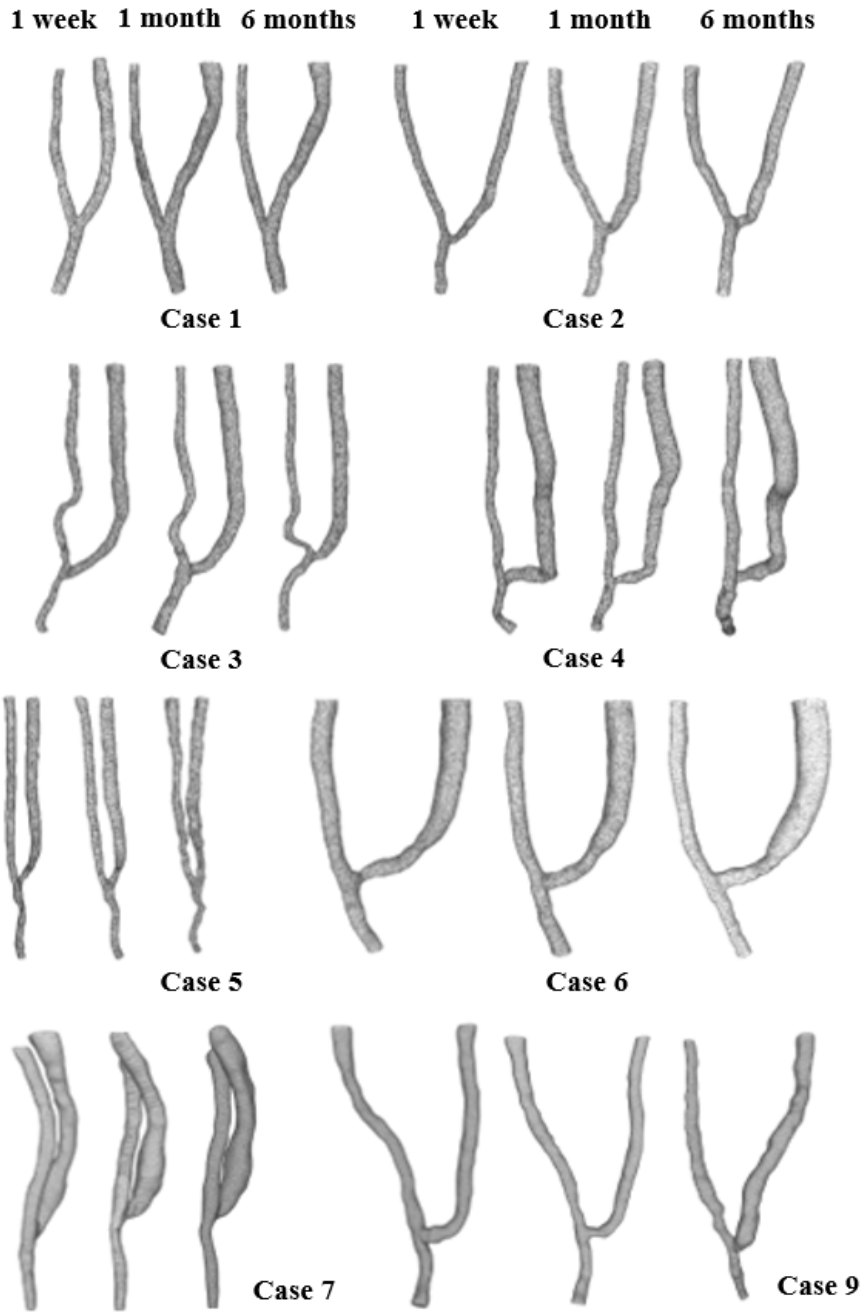

Figure 15: All the surface meshes of the patients involved in the study except for patient 8, which is already shown in Figure 6.

The sections that have been analyzed to obtain the results presented in the thesis are those shown in the Figure 16. The sections are extrapolated to the other AVFs, since they have been chosen as similar as possible in size and location.

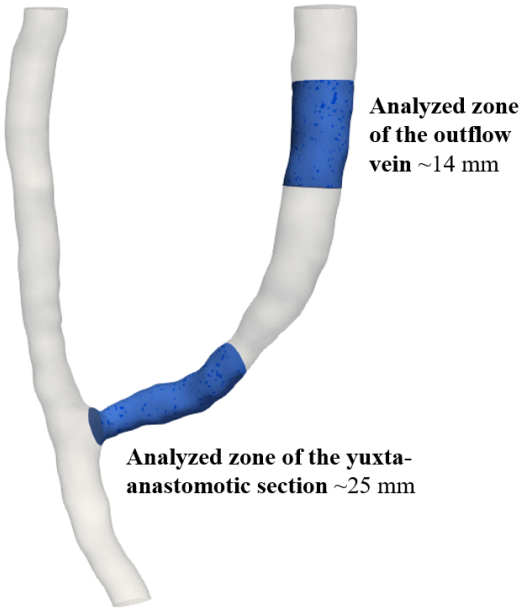

Figure 16: Sections of the juxta-nastomotic zone and outflow vein analyzed for drawing conclusions in this study.

A.1 Mesh convergence study

This section presents all the results that could not be included in the body of the thesis and that pertain to the mesh convergence study.

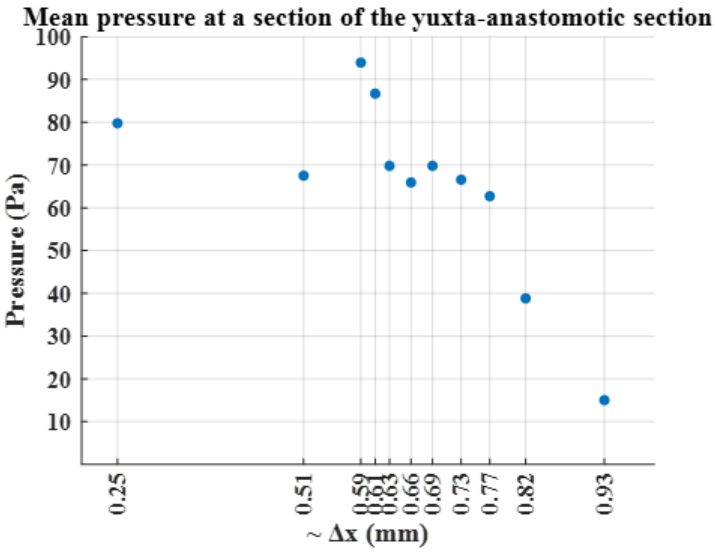

Figure 17: Average pressure results of the mesh convergence study for different mesh densities (i.e., Δx) in the yuxta-anastomotic zone.

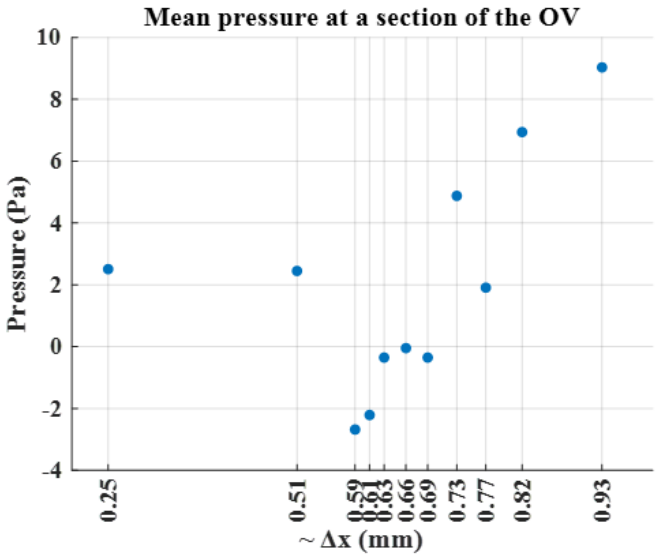

Figure 18: Average pressure results of the mesh convergence study for different mesh densities (i.e., Δx) in the outflow vein zone.

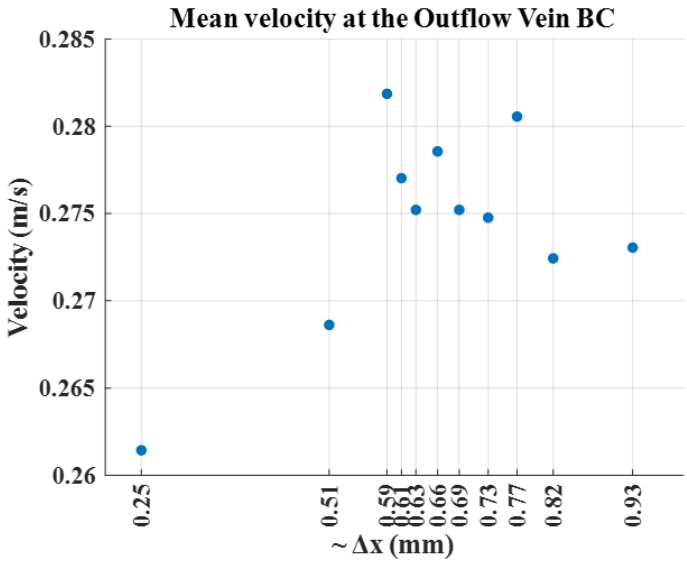

Figure 19: Average velocity results of the mesh convergence study for different mesh densities (i.e., Δx) in the outflow vein BC.

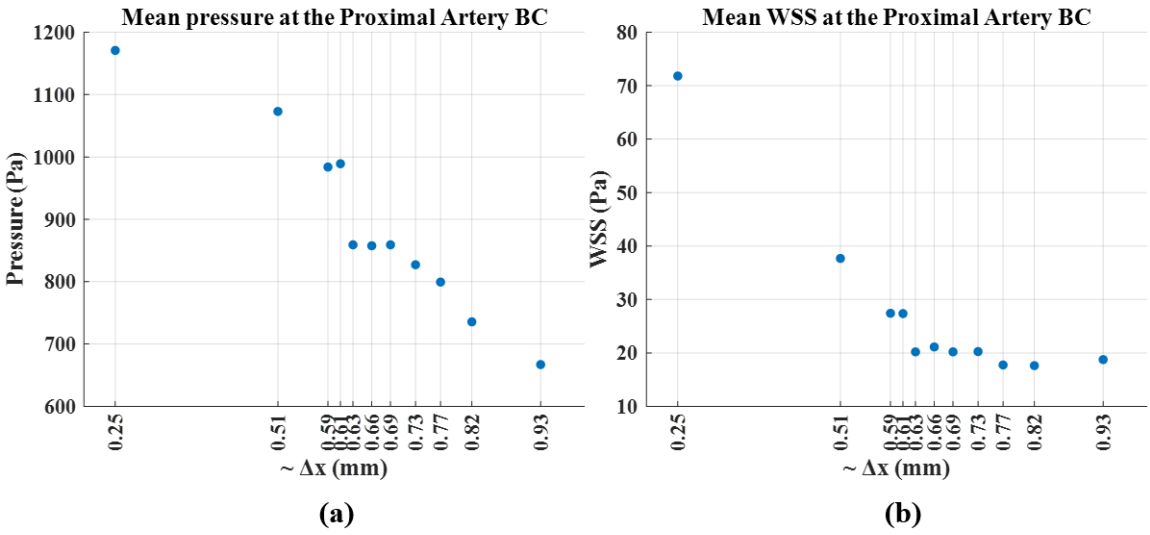

Figure 20: Average pressure and WSS results of the mesh convergence study for different mesh densities (i.e., Δx) at the proximal artery BC.

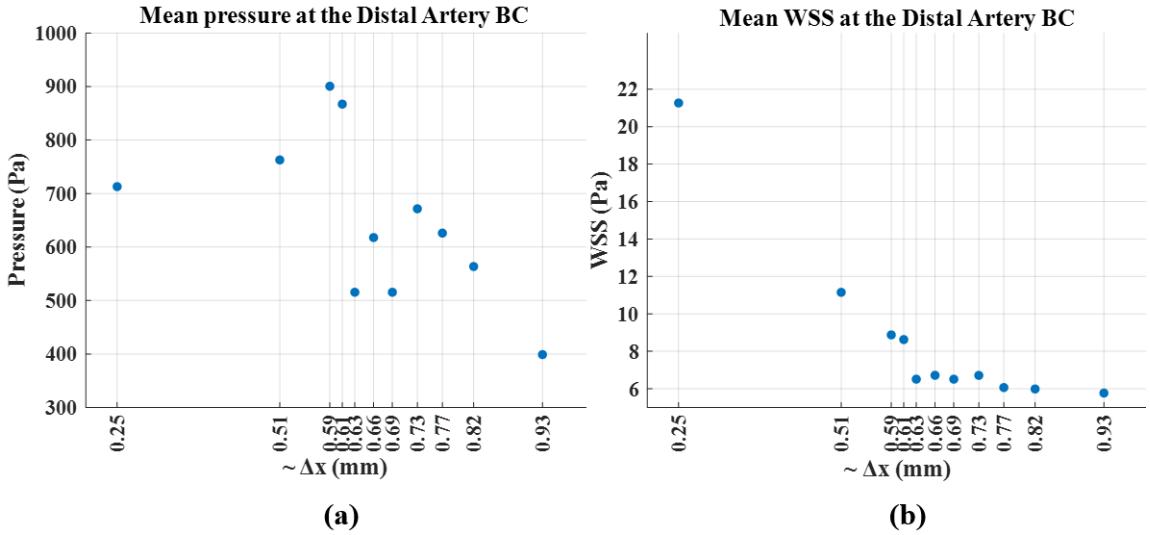

Figure 21: Average pressure and WSS results of the mesh convergence study for different mesh densities (i.e., Δx) at the distal artery BC.

A.2 Temporal follow-up simulations

Figure 22: Geometry of the AVF corresponding to patient 6, 1 week. In this, the pathlines depict the contribution of different segments of the artery (PA and DA) to the vein flow (OV). These illustrations demonstrate the flow split assumption applied in the contours, where PA contributes 75% of the flow to OV, and DA contributes 25%. The dynamics of the pathlines is almost the same for all cases and all simulated times due to the BCs applied.

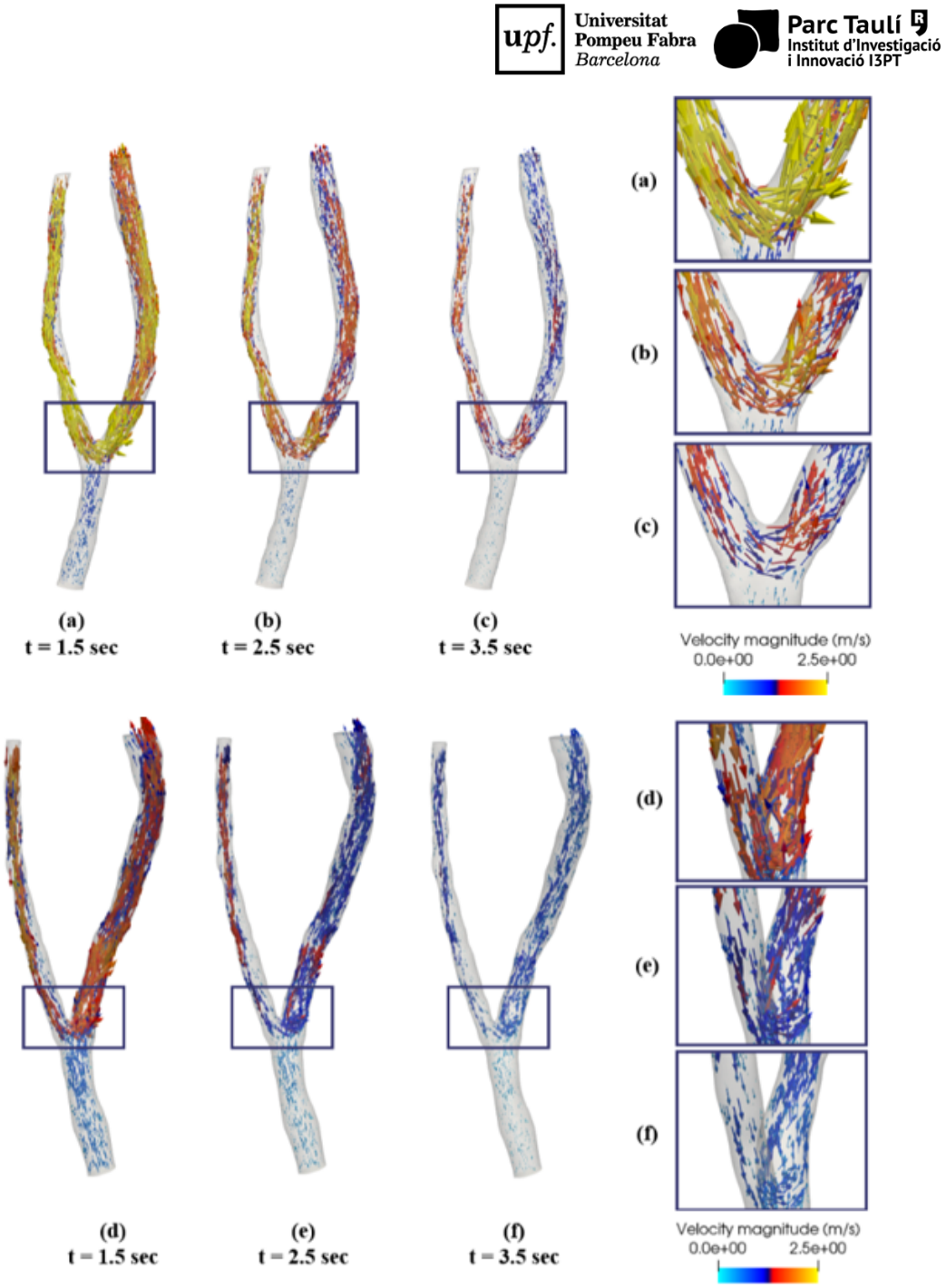

Figure 23: Magnitude of velocity vectors in AVF flow in Patient 1, week 1 (a, b, c) and month 1 (d, e, f). The results for the 6-month simulation are very similar to those of the 1-month simulation, so they have not been included to avoid redundancy. This extends to the other patient cases.

A.3 Training course certificate

The accurate identification of the structures for geometry segmentation was further enhanced through participation in the 21-hour theoretical-practical course 'Ultrasound for Vascular Access in Hemodialysis' held at Parc Taulí Hospital Universitari. Figure 24 depicts the certificate of attendance to such event.

Parc Taulí Institut d'Investigació i Innovació I3PT

CERTIFICADO

Los abajo firmantes certifican la asistencia de,

LIDIA MARTÍNEZ DALMAU

En el XVIII curso teórico-práctico:

Ecografía para el Acceso Vascular en Hemodiálisis

que se ha realizado en el Consorci Corporació Sanitària Parc Taulí de Sabadell del 20 al 22 de febrero de 2023, con un total de **21 horas** teórico-prácticas, y que ha sido acreditado por el Comité Institucional de Docencia, con el soporte de la Fundació Institut d'Investigació i Innovació Parc Taulí.

Dra. Josefa Rivera
Jefa de Estudios
Consorci Corporació Sanitària Parc Taulí

Dr. Lluís Blanch
Director Fundació Institut d'Investigació I Innovació Parc Taulí

Dr. José Ibeas
Coordinador del Curso

Dirigido a Médicos de Nefrología, Angiología y Cirugía Vascular y Radiodiagnóstico

Patrocinadores:

Avaladores:

"Activitat acreditada pel Consell Català de Formació Continuada de les Professions Sanitàries – Comisión de Formación Continuada del Sistema Nacional de Salud". 09/033995-MD. Crèdits: 4.2

Els crèdits d'aquesta activitat formativa no són aplicables als professionals que hi participen i que estan formant-se com a especialistes en Ciències de la Salut

Figure 24: Theoretical-practical course 'Ultrasound for Vascular Access in Hemodialysis' certificate of attendance.